Bioactive Materials 47 (2025) 327–342

Contents lists available at ScienceDirect

Bioactive Materials

journal homepage: www.keaipublishing.com/en/journals/bioactive-materials

Photo-generating Type-I ROS and aryl radicals by mitochondrial-targeting oxime-ester photogenerator for pyroptosis-mediated anti-hypoxia photoimmunotherapy

Qiyu Zhan [a,1], Yulin Kuang [b,e,c,1], Xuyuan Chen [b,f,c,1], Yanzhen Yang [b,c,1], Linhui Jiang [b,c], Jian Chen [a], Lie Li [a], Junwei Wang [g], Shuoji Zhu [b,c,*****], Huanlei Huang [b,c,h,****], Lei Wang [d,***], Ping Zhu [b,c,h,**], Ruiyuan Liu [a,*]

[a] Biomaterials Research Center, School of Biomedical Engineering, Southern Medical University, Guangzhou, 510515, China
[b] Guangdong Cardiovascular Institute, Guangdong Provincial People's Hospital (Guangdong Academy of Medical Sciences), Southern Medical University, Guangzhou, Guangdong, 510100, China
[c] Guangdong Provincial Key Laboratory of Pathogenesis, Targeted Prevention and Treatment of Heart Disease, Guangzhou Key Laboratory of Cardiac Pathogenesis and Prevention, Guangzhou, Guangdong, 510100, China
[d] College of Materials and Chemical Engineering, Key Laboratory of Inorganic Nonmetallic Crystalline and Energy Conversion Materials, China Three Gorges University, Yichang, 443002, China
[e] School of Medicine, South China University of Technology, Guangzhou, Guangdong, 510006, China
[f] Comprehensive Medical Treatment Ward, Nanfang Hospital, Southern Medical University, Guangzhou, 510515, China
[g] Department of Cardiovascular Surgery, Nanfang Hospital, Southern Medical University, Guangzhou Avenue North No. 1838, Baiyun District, Guangzhou, 510515, China
[h] Guangdong Provincial People's Hospital Ganzhou Hospital, Ganzhou, 341000, China

ARTICLE INFO

Keywords:
Pyroptosis
Type-I photodynamic therapy
Photoimmunotherapy
Photolysis reaction
Oxime ester

ABSTRACT

Pyroptosis is an inflammatory form of programmed cell death with great potential in cancer immunotherapies. Photodynamic therapy (PDT) represents a promising treatment modality to trigger pyroptosis. However, the hypoxic microenvironment inside the tumors often induces limited therapeutic efficacy. Herein, in this work, the first type of mitochondrial-targeting oxime-ester photogenerator (T-Oximer) was constructed to boost type-I ROS/aryl free radicals which could induce DNA damage by DNA cleaving and facilitate high-efficiency pyroptosis-mediated photoimmunotherapy. Detailed mechanism investigations revealed that T-Oximer could produce aryl free radicals *via* photolysis reaction and generate type-I ROS ($O_2^{\bullet-}$ and •OH) based on the type-I electron transfer process. Meanwhile, T-Oximer could accumulate in the mitochondria, boost mitochondrial radicals, and damage mitochondria in hypoxic tumor cells. Of peculiar interest, T-Oixmer could bind with DNA and cleave DNA to induce DNA damage. Combined mitochondrial damage with DNA cleavage, T-Oximer can initiate pyroptosis, activate the ICD effect, and trigger robust systemic antitumor immunity for efficient tumor regression

Peer review under the responsibility of KeAi Communications Co., Ltd.
* Corresponding author. Biomaterials Research Center, School of Biomedical Engineering, Southern Medical University, Guangzhou, 510515, China.
** Corresponding author. Guangdong Cardiovascular Institute, Guangdong Provincial People's Hospital (Guangdong Academy of Medical Sciences), Southern Medical University, Guangzhou, Guangdong, 510100, China.
*** Corresponding author. College of Materials and Chemical Engineering, Key Laboratory of Inorganic Nonmetallic Crystalline and Energy Conversion Materials, China Three Gorges University, Yichang, 443002, China.
**** Corresponding author. Guangdong Cardiovascular Institute, Guangdong Provincial People's Hospital (Guangdong Academy of Medical Sciences), Southern Medical University, Guangzhou, Guangdong, 510100, China.
***** Corresponding author. Guangdong Cardiovascular Institute, Guangdong Provincial People's Hospital (Guangdong Academy of Medical Sciences), Southern Medical University, Guangzhou, Guangdong, 510100, China.
E-mail addresses: zhushuoji@gmail.com (S. Zhu), huanghuanlei@gdph.org.cn (H. Huang), lei.wang@ctgu.edu.cn (L. Wang), tanganqier@163.com (P. Zhu), ruiyliu@smu.edu.cn (R. Liu).
[1] These authors contributed equally to this work.

https://doi.org/10.1016/j.bioactmat.2025.01.032
Received 15 December 2024; Received in revised form 23 January 2025; Accepted 23 January 2025

and metastasis suppression. Our finding provides a new strategy for constructing oxygen-independent photogenerator for high-efficiency pyroptosis-mediated anti-hypoxia photoimmunotherapy.

1. Introduction

Pyroptosis represents a novel mode of programmed cell death (PCD), which is initiated by the Gasdermin family and characterized by cell membrane rupture, cell swelling with discernible bubbles, and eventual cell lysis [1–3]. Pyroptosis occurs more rapidly, and its lytic properties facilitate the release of proinflammatory cytokines and intracellular damage-associated molecular patterns (DAMPs), which can induce ICD, enhance immune response, and remodel the immunosuppression microenvironment [4–6]. These features suggest that the induction of pyroptosis in tumor cells may offer a promising avenue for developing efficacious cancer immunotherapies [7–9]. However, pyroptosis is predominantly triggered by chemotherapeutic drugs, which are prone to drug resistance, instability, inadequate expression, and associated with severe adverse effects. It is therefore essential to investigate new approaches to induce pyroptosis to treat tumors.

Photodynamic therapy (PDT) represents a promising therapeutic approach for treating cancers, wherein photosensitizers (PSs) are triggered by light irradiation to generate cytotoxic reactive oxygen species (ROS), initiating PCD and ultimately leading to the death or necrosis of tumor cells [10–13]. Due to its safety, specificity, and reproducibility, PDT has attracted considerable attention in the biomedical field [14–16]. However, there are still several challenges for clinical applications. Firstly, the hypoxic tumor microenvironment (TME, $pO_2 < 5$ mm Hg) significantly inhibits ROS production, thereby diminishing the effectiveness of PDT to induce pyroptosis. Recently, type-I photosensitizers, which generate $O_2^{\bullet-}$ or •OH *via* type-I electrons transferring process with a low oxygen-dependent performance, demonstrated an exceptional capacity to overcome the constraints and displayed great performance in treating hypoxic cancer [17–19]. To further promote the oxygen-independent ability toward the treatment against hypoxia tumors, oxygen-independent radicals are boosted by thermal decomposable azo initiators through the photothermal therapy (PTT) process [20–23]. However, the current multicomponent systems often suffer from complexity, instability, and inappropriateness, leading to limited clinical application. Oxime esters can effectively generate alkyl/aryl free radicals upon light irradiation by homolytic cleavage of the N-O bond [24–26]. Furthermore, oxime ester demonstrated a remarkable affinity for DNA, exhibiting the capacity to bind to DNA *via* intercalation [27–29]. More significantly, oxime esters could cleave DNA when exposed to light of an appropriate wavelength [30,31]. As DNA photocleavers, oxime esters have the potential to damage DNA and induce pyroptosis, which represents a promising avenue for the development of pyroptosis inducers. Consequently, combined type-I photosensitizers with oxime ester have a great potential to enhance the treatment efficacy for pyroptosis-mediated photoimmunotherapy toward hypoxia tumors.

Another critical challenge is the inherent flow of free radicals through PDT process, which has a very short lifespan (0.03–0.18 ms) and a small diffusion range (<20 nm). The temporary attenuation of ROS has significantly compromised the therapeutic efficiency of PDT. Therefore, the precise accumulation of photosensitizers in subcellular organelles is crucial to improving PDT efficacy [32–36]. Mitochondria, the control center of cell apoptosis and the powerhouse of cells are involved in many biological processes. Mitochondria dysfunction may result in a variety of diseases, such as neurodegenerative disorders, metabolic diseases as well as cancer [37–39]. More significantly, the increased mitochondrial reactive free radicals have the potential to activate gasdermine and trigger cell pyroptosis [40,41]. Consequently, the development of mitochondrial targeting photogenerators would be advantageous, because it can boost ROS production in mitochondria and precisely damage them to trigger pyroptosis-mediated photoimmunotherapy for hypoxic tumors.

To overcome the aforementioned problems, we present an approach whereby visible light absorptive photosensitizers are structurally modified with oxime ester groups to prepare mitochondrial targeting type-I ROS/aryl free radicals combined photogenerator for pyroptosis-mediated anti-hypoxia photoimmunotherapy (Scheme 1). In this contribution, we employed triphenylamine, thiophene, and benzo-2,1,3-thiadiazole groups to prepare a π-conjugated photosensitive chromophore, which was then modified with an oxime ester group to obtain the corresponding oxime ester (T-Oximer). When exposed to LED white light, T-Oximer can generate aryl free radicals *via* photolysis reaction and produce type-I ROS ($O_2^{\bullet-}$ and •OH) through type-I photodynamic process. T-Oximer displays an excellent subcellular distribution on the mitochondria, which could effectively enhance mitochondrial ROS *in situ* upon illumination, depolarize MMP, and induce mitochondrial damage. Moreover, T-Oximer could bind and cleave DNA, which triggers DNA damage. Furthermore, T-Oximer could activate pyroptosis, initiate the ICD effect, and initiate potent systemic antitumor immunity to inhibit tumor growth and suppress metastasis. Thus, as the first example of a type-I ROS/aryl free radicals combined photogenerator, T-Oximer provides an efficient pyroptosis-mediated photoimmunotherapy for treating hypoxic tumors.

2. Materials and methods

2.1. Synthesis of T-Oximer

T-Oxi (1.008 g, 2 mmol) was added into CH_3CN (10 mL) and Et_3N (1 mL). Under ice water baths, benzoyl chloride (280 mg, 2 mmol) was drop added. The reaction was carried out overnight. The solvent was evaporated in a vacuum, and the resulting mixture was dissolved in DCM. The organic solution was washed with brine water and dried in a vacuum drier. The obtained residue was purified by gel column chromatography with dichloromethane/methanol (from 50:1 to 20:1) as eluent, giving to the desired product as red solid (382 mg), yielding 49 %. ^{1}H NMR (600 MHz, $CDCl_3$) δ 7.91–7.94 (t, 2H), 7.80–7.82 (m, 3H), 7.66–7.67 (t, 2H), 7.62 (d, J = 7.2 Hz, 1H), 7.21–7.24 (m, 6H), 7.11–7.15 (m, 9H), 6.98–7.03 (m, 3H). ^{13}C NMR (300 MHz, $CDCl_3$) 154.17, 153.72, 152.54, 148.66, 147.99, 147.50, 147.26, 146.39, 137.71, 134.63, 132.17, 131.02, 130.05, 129.90, 129.45, 129.37, 127.20, 126.66, 126.10, 125.17, 124.90, 123.66, 123.31, 122.95, 122.43. ESI-HRMS *m/z*: calcd. for $C_{36}H_{25}N_4S_2^+$ $[M - H]^+$ 609.1413, found: 609.1414.

2.2. The detection of singlet oxygen generated from T-oximer NPs via ABDA

9,10-Anthracenediyl-bis(methylene)-dimalonic acid (ABDA) is used to monitor $^1O_2$ production. The concentrations of ABDA and T-Oximer NPs in their aqueous mixture were 100 μM and 10 μM, respectively. The above solution is irradiated with an LED white light (60 mW/cm^2) for different periods of time. The change in the absorption signal of the indicator ABDA at 380 nm was monitored by an ultraviolet–visible spectrometer to monitor the generation of $^1O_2$.

2.3. The detection of ROS generated from T-oximer NPs via DCFH

2′,7′-Dichlorodihydrofluorescein (DCFH), which was obtained from 2′,7′-dichlorodihydrofluorescein diacetate (DCFH-DA), was used as the probe to evaluate ROS generation. The concentrations of DCFH and T-

Oximer NPs in their aqueous mixture were 10 μM and 10 μM, respectively. The above solution is irradiated with an LED white light (60 mW/cm^2) for different periods of time. The change in the fluorescence signal of DCFH is monitored by a fluorescence spectrometer. The excitation wavelength is 480 nm, and the fluorescence intensity of DCFH at 525 nm is recorded to indicate ROS generation. A curve was drawn to compare the fluorescence changes of DCFH in different solutions, so as to obtain the difference in ROS generation capacity.

2.4. The detection of singlet oxygen generated from T-oximer NPs via SOSG

Specific single oxygen sensor green (SOSG) is used as an indicator of $^1O_2$. The concentrations of SOSG and T-Oximer NPs in their aqueous mixture were 5 μM and 10 μM, respectively. The above solution is irradiated with an LED white light (60 mW/cm^2) for different periods of time. The change in the fluorescence signal of SOSG is monitored by a fluorescence spectrometer. The excitation wavelength used is 480 nm, and the fluorescence intensity of SOSG at 525 nm is recorded to evaluate $^1O_2$ generation.

2.5. The detection of superoxide anion radical ($O_2^{\bullet-}$) generated from T-oximer NPs via DHR123

Dihydrorhodamine 123 (DHR123) is used as an indicator of $O_2^{\bullet-}$, which can be converted to rhodamine 123 in the presence of $O_2^{\bullet-}$. The concentrations of DHR123 and T-Oximer NPs in their aqueous mixture were 10 μM and 10 μM, respectively. The above solution is irradiated with an LED white light (60 mW/cm^2) for different periods of time. The change in the fluorescence signal of the DHR123 is detected by a fluorescence spectrometer. The excitation wavelength used is 480 nm, and the fluorescence intensity of DHR123 at 525 nm is recorded to indicate superoxide anion radical generation.

2.6. The detection of hydroxyl radical (•OH) generated from T-oximer NPs via TMB

3,3′,5,5′-Tetramethylbenzidine dihydrochloride (TMB) is used to monitor •OH production. The concentrations of TMB and T-Oximer NPs in their aqueous mixture were 30 μM and 10 μM, respectively. The above solution is irradiated with an LED white light (60 mW/cm^2) for different periods of time. The change in the UV absorption signal of TMB-OX is monitored by a UV–vis spectrometer. The change in the absorption signal of TMB-OX at 425 nm was monitored by an ultraviolet–visible spectrometer to monitor the generation of •OH.

2.7. The detection of hydroxyl radical (•OH) generated from T-oximer NPs via HPF

Hydroxyphenyl fluorescein (HPF) is used to monitor •OH production. The concentrations of HPF and T-Oximer NPs in their aqueous mixture were 5 μM and 10 μM, respectively. The change in the fluorescence signal of HPF is detected by a fluorescence spectrometer. The excitation wavelength used is 480 nm, and the fluorescence intensity of HPF at 520 nm is recorded to indicate •OH generation.

2.8. ROS generated from PDT detection with electron paramagnetic resonance (EPR)

DMPO was used as a trapping agent for •OH and $O_2^{\bullet-}$. The T-Oximer

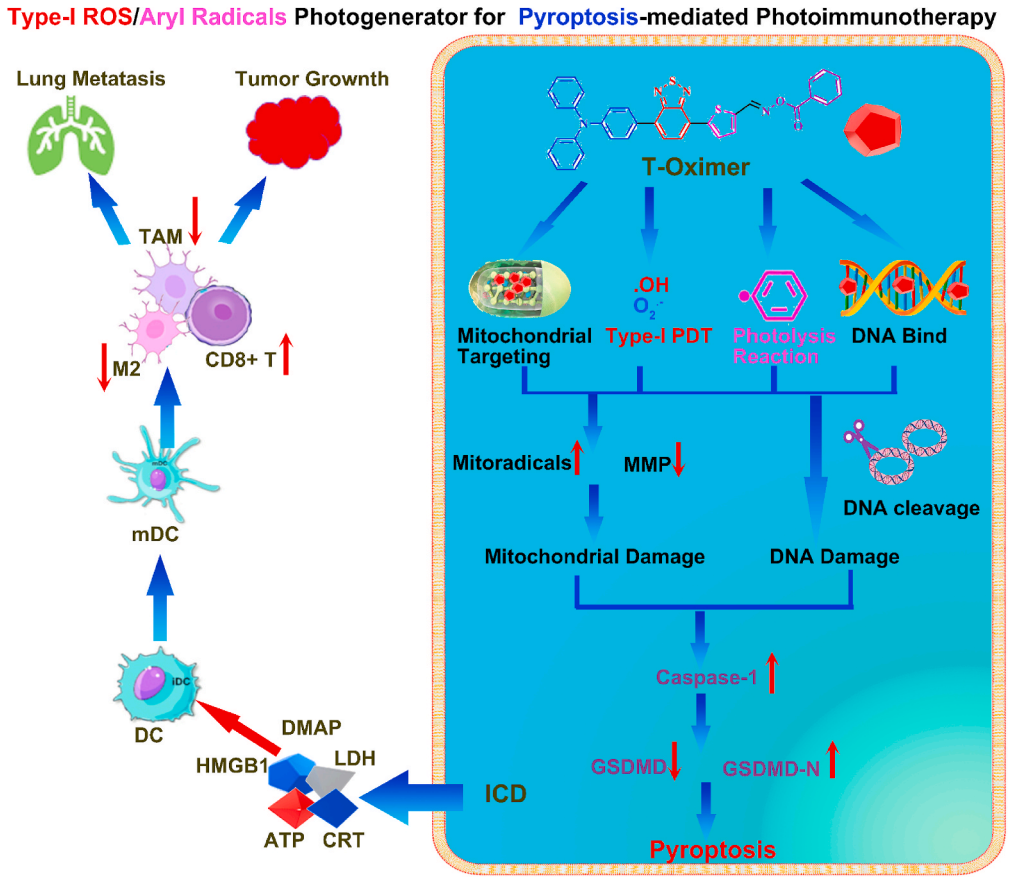

Scheme 1. Schematic illustration of mitochondrial targeting type-I ROS/Aryl free radicals combined photogenerator for pyroptosis-mediated anti-hypoxia photoimmunotherapy.

were respectively dissolved in H_2O/DMSO (V_{water}/V_{DMSO} = 99:1) mixed solution. DMPO was dissolved in CH_3OH or DMSO, which was further added into T-Oximer aqueous solution to reach a final concentration of 100 μM and 10 μM for DMPO and T-Oximer, respectively. The EPR spectra of the mixtures were recorded before and after light irradiation (LED white light, 10 min, 60 mW/cm^2). The electron paramagnetic resonance (EPR, Bruker A300) spectra were measured to evaluate ROS generation. For comparison, DMPO + T-Oximer (10 μM) group was tested by an electron paramagnetic resonance spectrometer.

2.9. Aryl free radical (•phenyl) detection via ABTS

2,2′-Azinobis-(3-ethylbenzthiazoline-6-sulphonate) (ABTS) was used as indicator for detection of •phenyl in aqueous solution. The concentrations of ABTS and T-Oximer NPs in their aqueous mixture were 30 μM and 10 μM, respectively. The above solution is irradiated with an LED white light (60 mW/cm^2) for different periods of time. The change in the UV absorption signal of ABTS is monitored by a UV–vis spectrometer. The change in the absorption signal of ABTS+• at 740 nm was monitored by an ultraviolet–visible spectrometer to monitor the generation of •phenyl.

2.10. Aryl free radical (•phenyl) generated from photolysis reaction detection with electron paramagnetic resonance (EPR)

PBN and POBN were used as trapping agents for phenyl. T-Oximer was respectively dissolved in H_2O/DMSO (V_{water}/V_{DMSO} = 99:1) mixed solution. Trapping agents were dissolved in DMSO, which was further added into T-Oximer aqueous solution to reach a final concentration of 100 μM and 10 μM for trapping agent and T-Oximer, respectively. The EPR spectra of the mixtures were recorded before and after light irradiation (LED white light, 10 min, 60 mW/cm^2). For comparison, PBN + T-Oxi (10 μM) group, PBN + Con-Oximer (10 μM) group, POBN + T-Oxi (10 μM) group, and POBN + Con-Oximer (10 μM) group were tested by an electron paramagnetic resonance spectrometer.

2.11. Construction of tumor models

Five weeks old female BALB/c mice were provided by the Animal Center of Southern Medical University. All animal experiments were carried out under the guidance of the protocols approved by the local Ethical Committee in compliance with the Chinese law on experimental animals and followed the regulations of the Institutional Animal Care and Use Committee of South Medical University (SCXK 2016–0041). All mice were kept in SPF-level feeding conditions with adequate water and food. The temperature is kept at 26 °C, the humidity is 50 % and a 12 h light/dark cycle.

2.12. Statistical analysis

Unpaired two-tailed Student's *t*-test was used to compare the statistical significance between two data groups. One-way analysis of variance (ANOVA) with a Bonferroni post hoc test was used to compare three or more groups. Quantitative data were indicated as mean ± S.D. Asterisks were used to represent significant differences (n.s.: no significance, *P < 0.05). The statistical analysis was performed by using GraphPad Prism 8.0 software.

3. Results and discussions

3.1. Molecular design and photophysical properties of T-oximer NPs

To obtain excellent visible-light excitation photoinitiators, chromophores with a conjugated structure for visible-light absorption are essential. The D-A-*π* structure photosensitive chromophore (TBT) was fabricated with intramolecular charge transfer (ICT) characteristics. Triphenylamine was selected as the D moiety because of its excellent charge transfer capabilities, strong electron-donating capacity, and good photostability. The benzo-2,1,3-thiadiazole moiety served the function of the A part to facilitate triplet sensitization. Moreover, the thiophene unit was used as a π-bridge to prolong the conjugation and improve the capacity to donate electrons. The oxime ester structure was successfully introduced to construct the visible light-excited oxime ester derivatives (T-Oximer) (Fig. 1a). The structures of the T-Oximer were characterized using ^{1}H NMR, ^{13}C NMR, mass spectrometry (HRMS) (Figs. S1–S5, supporting information).

To enhance biosafety and biocompatibility, the hydrophobic T-Oximer was encapsulated into DSPE-PEG2000 to provide corresponding T-Oximer nanoparticles (T-Oximer NPs). As illustrated in Fig. 1b and c, the transmission electron microscope (TEM) image and dynamic light scattering (DLS) analysis revealed that the T-Oximer NPs exhibited uniform morphology with a particle size around 100 nm. Furthermore, the particle size stability of the T-Oximer NPs at different time points was evaluated using DLS, which exhibited minimal variation over two weeks in serum (Fig. S6, supporting information). Moreover, no discernible alterations in TEM morphology were observed following a 28-day incubation period (Fig. S7, supporting information), thereby reinforcing the stability of T-Oximer NPs. The photophysical characteristics of T-Oximer NPs were investigated *via* UV–vis absorption and fluorescence spectroscopy. As shown in Fig. 1d, the absorption and emission spectra of T-Oximer NPs exhibited an absorption peak at approximately 490 nm with high molar extinction ecoefficiency (ε = 1.131 × 10^4 mol cm^{-1}·L^{-1}) and a fluorescence emission peak at 690 nm, confirming that T-Oximer NPs are suitable for NIR fluorescent imaging.

Subsequently, density functional theory (DFT) and time-dependent density functional theory (TD-DFT) calculations were employed to investigate the photophysical and electronic characteristics of T-Oximer. The calculated frontier molecular orbitals (FMOs) are depicted in Fig. 1e. A distinct separation between the highest occupied molecular orbital (HOMO) and the lowest occupied molecular orbital (LUMO) was observed in T-Oximer, indicating a pronounced ICT character. The HOMO was primarily localized at the triphenyl group, while the LUMO was distributed around the benzo-2,1,3-thiadiazole unit. The energy gap between the HOMO and LUMO was calculated to be 4.744 eV. Meanwhile, the energy gap ($\Delta E_{S1\text{-}Tn}$) below 0.3 eV is a decisive factor for the efficient intersystem crossing (ISC) process, which is beneficial for improving the PDT effect [42]. Fig. 1f displayed that the energy gap between S_1 and the nearest T_2 ($\Delta E_{S1\text{-}T2}$ = 0.23) is evidently less than 0.3 eV, and this quite small energy gap could induce the ISC process to occur from S_1 to T_2 for T-Oximer effortlessly. Moreover, T-Oximer possesses a low energy level of T_1 state (<1.61 eV), which can minimize the energy transfer pathway, thereby enhancing the efficacy Type I process [43].

3.2. The $O_2^{\bullet-}$ and •OH generation from T-oximer NPs via Type-I photodynamic effect

Previous research confirmed that the D-A-π structured TBT directives exhibited excellent photodynamic effects. We then investigated the photodynamic properties of T-Oximer NPs. The total ROS-generating abilities of T-Oximer NPs were meticulously examined using 2′,7′-dichlorofluorescin (DCFH) as an indicator. To verify the molecular design strategy, T-Oxi and Con-Oximer were selected as the control samples (Fig. 2a). To our delight, the fluorescence intensity of DCFH significantly increased 83.2-fold in the presence of T-Oximer NPs when exposed to LED white light for 60s (Fig. 2b; Fig. S8, supporting information), much higher than that of T-Oxi (8.5-fold). To verify the type-I ROS generation ability of T-Oximer NPs, commercial dihydrorhodamine 123 (DHR123), hydroxyphenyl fluorescein (HPF), and TMB were selected as indicators to evaluate the superoxide anion ($O_2^{\bullet-}$), and hydroxide radicals (•OH) generation ability of T-Oximer NPs. Following a radiation exposure of 60 s, the fluorescence intensity of DHR123 enhanced 60.0-fold in presence of T-Oximer NPs (Fig. 2c; Fig. S9,

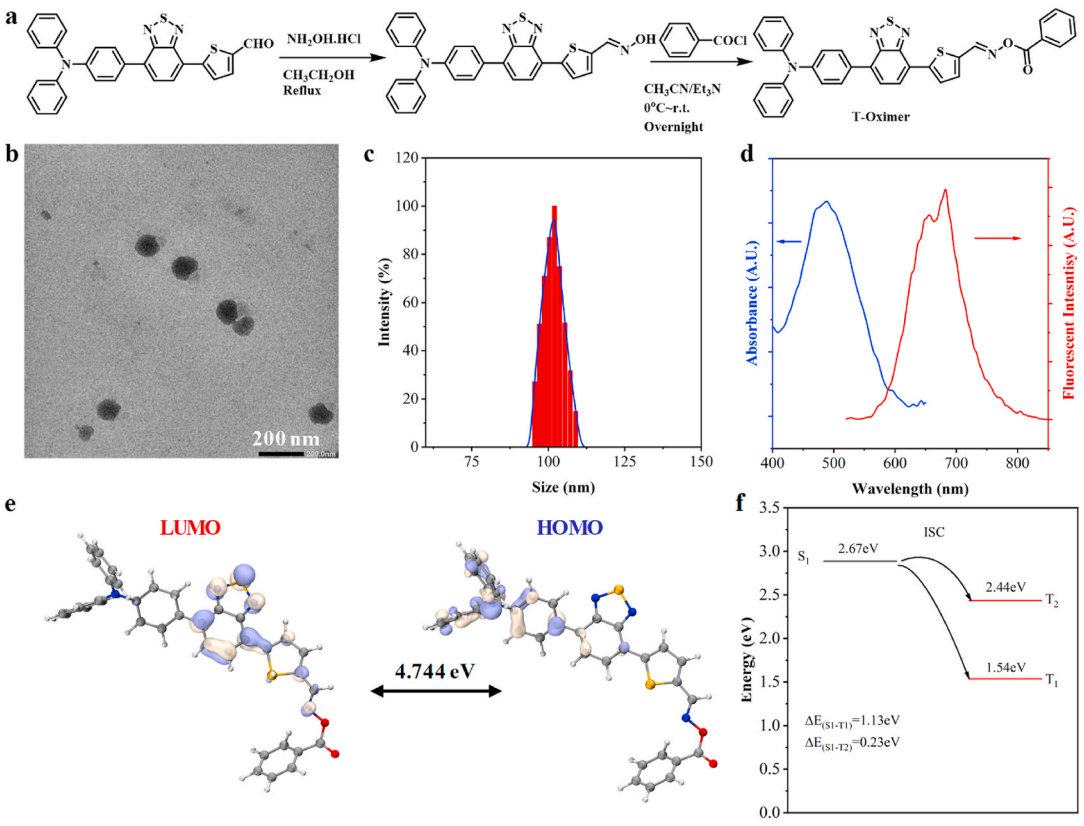

Fig. 1. (a) The preparation routine of T-Oximer. (b) The TEM of T-Oximer NPs. (c) The DLS of T-Oximer NPs. (d) The UV–vis and fluorescent spectrum of T-Oximer NPs. (e) Calculated HOMO and LUMO of T-Oximer. (f) The energy gap of T-Oximer.

supporting information). Moreover, upon illumination with white LED light, a discernible 11.9-fold enhancement of HPF fluorescence intensity was observed, indicating the production of •OH (Fig. 2d; Fig. S10, supporting information). The same outcomes were attained when TMB was employed to monitor •OH generation (Fig. 2e; Fig. S11, supporting information). As a comparison, T-Oxi depicted the ROS generation ability to some extent. Conversely, no obvious ROS was detected in presence of Con-Oximer, suggesting that the D-A-π -structured benzo-2,1,3-thiadiazole structure was essential for ROS generation. Then, to determine T-Oximer NPs tended to generate the type-I ROS through the electron transfer process, 9,10-anthracenediylbis (methylene)-dimalonic acid (ABDA) and singlet oxygen sensor green (SOSG) are employed as $^1O_2$ indicators. As illustrated in Fig. 2f and Fig. S12 (supporting information), the absorption of ABDA exhibits minimal attenuation, reaching ultrasmall decrease after 60 s irradiation. Additionally, a similar result was observed with SOSG, as substantiated by its fluorescence intensity hardly varying as the exposure time was prolonged (Fig. S13, supporting information). In light of the distinctive benefits of the type-I photodynamic effect in hypoxic environments, an in-depth examination of T-Oximer's photodynamic performance was further conducted. The fluorescence intensity of DHR123 probes rises steadily during LED light irradiation (Fig. S14, supporting information), which is attributed to the unaffected generation of $O_2•^-$ by oxygen concentration. Furthermore, in a hypoxic environment, HPF demonstrated a sustained increase in fluorescence during LED light irradiation (Fig. S15, supporting information), indicating that the generation of •OH remained unimpaired. Due to its high cytotoxicity and low oxygen dependence, •OH has attracted significant attention in photodynamic process. The capacity of T-Oximer NPs to produce •OH in various circumstances was assessed (Fig. 2g; Fig. S16, supporting information). The addition of NaN_3 ($^1O_2$ quencher) or H_2O_2 did not affect the fluorescence enhancement of HPF, indicating that the formation of •OH was not dependent on $^1O_2$ and H_2O_2. The purging of the solution with nitrogen resulted in a notable reduction in the formation of •OH, indicating that oxygen remains a vital component in the generation of •OH in type-I PDT. Taken together, the above results suggest that T-Oximer NPs is a type I PS with outstanding type-I ROS generation ability.

To further confirm the type of ROS, electron spin resonance (ESR) spectroscopy experiments were conducted using 5,5-dimethyl-1-pyrroline N-oxide (DMPO) as a radical trapping agent. As illustrated in Fig. 2h, the resulting EPR spectrum in the presence of DMPO and T-Oximer NPs upon white light irradiation exhibited a characteristic 2:2:1:2:1:2 six-signal pattern, which is the defining resonance for the DMPO/$O_2^{•-}$ adduct. Furthermore, four-line resonances with an intensity ratio of 1:2:2:1 were observed, which is characteristic of the DMPO/•OH adduct. These findings suggest that T-Oximer NPs may produce cytotoxic $O_2^{•-}$ and •OH *via* a type-I photodynamic process upon LED white light irradiation (Fig. 2i), indicating its potential as a type-I PS for phototheranostics in biomedical applications.

3.3. *The aryl free radical generation from T-oximer via photolysis reaction*

Photoinitiators could absorb the energy of light and transfer the light energy to generate free radicals that initiate the free radical polymerization process which attracted much attention in biomedical field [44–47]. Oxime ester, a kind of photoinitiators, can be triggered under LED light irradiation to generate an alkyl/aryl free radical *via* a photolysis reaction [48]. ABTS was employed as an indicator to investigate the ability of T-Oximer NPs to generate aryl radicals. As displayed in Fig. 3a and Fig. S17 (supporting information), the generation of ABTS+• displayed a time-dependent manner when ABTS was incubated with T-Oximer NPs upon LED white light irradiation. The ABTS+• concentration increased with the extended duration of LED white light

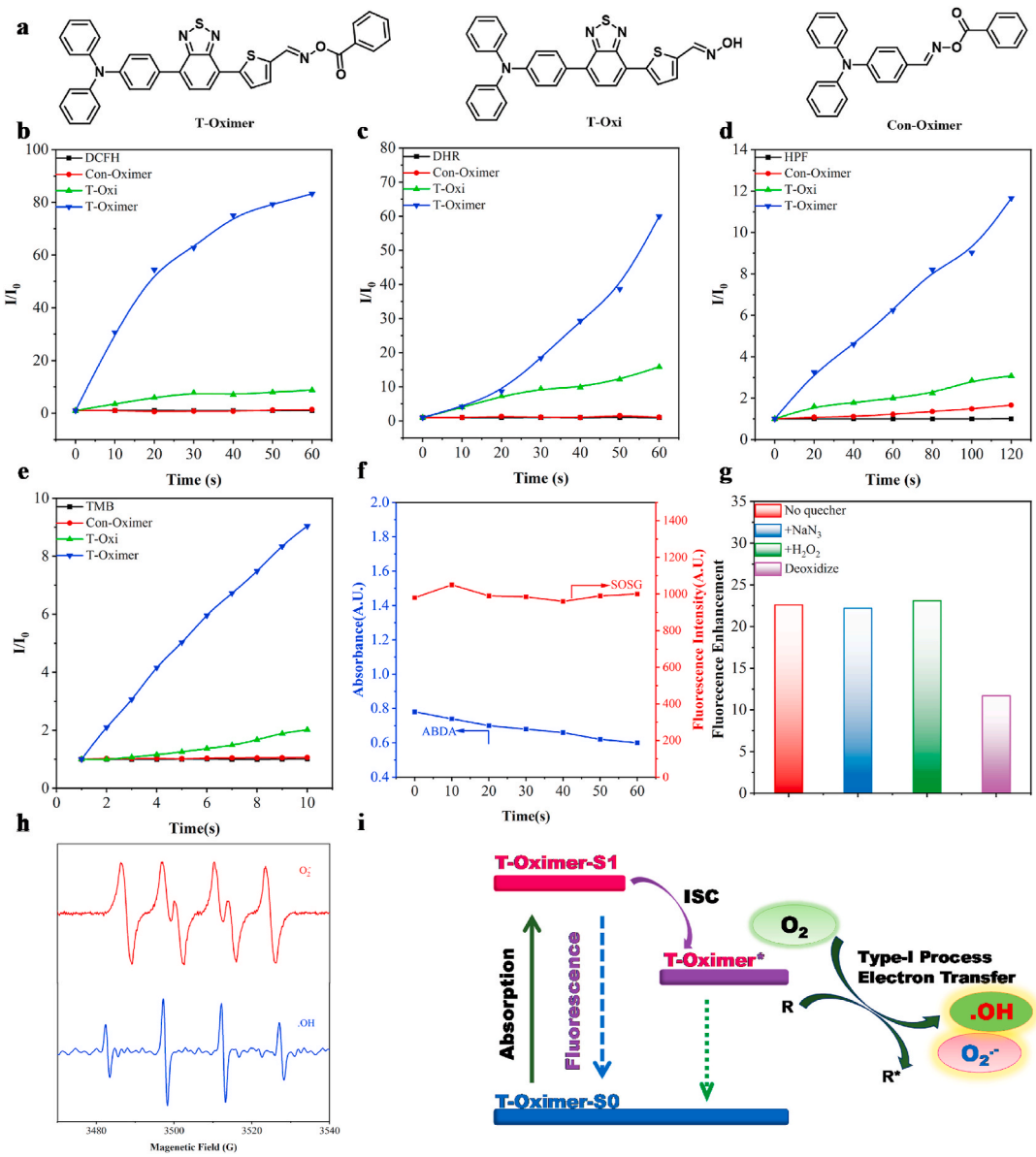

Fig. 2. (a) Structures of photogenerator (T-Oximer NPs, T-Oxi, and Con-Oximer). (b) Fluorescence enhancement of DCFH at 525 nm in the presence of T-Oximer NPs, T-Oxi, and Con-oximer under LED light irradiation (60 mW/cm^2). (c) Fluorescence enhancement of DHR123 at 525 nm in the presence of T-Oximer NPs, T-Oxi, and Con-Oximer under LED light irradiation (60 mW/cm^2. (d) Fluorescence enhancement of HPF at 520 nm in the presence of T-Oximer NPs, T-Oxi, and Con-oximer under LED light irradiation (60 mW/cm^2). (e)The absorption enhancement of TMB at 425 nm in the presence of T-Oximer NPs, T-Oxi, and Con-Oximer under LED light irradiation (60 mW/cm^2). (f) The fluorescence intensity of Singlet Oxygen Sensor Green (SOSG) and absorption of ABDA for $^1O_2$ detection, respectively. (g) Fluorescence enhancement of HPF (5 μM) in the presence of T-Oximer NPs (10 μM) and different additives (NaN_3, H_2O_2, N_2) under LED light irradiation (60 mW/cm^2). (h) ESR spectra of $O_2^{\bullet-}$ and •OH generation from T-Oximer under LED light irradiation (60 mW/cm^2). (i) Illustration of $O_2^{\bullet-}$ and •OH generation of T-Oximer *via* type-I process.

irradiation. As a comparison, T-Oxi and Con-Oximer depicted the aryl free radical generation ability to some extent, suggesting that the oxime or its ester units was essential for aryl free radical generation. Especially, the oxime ester derivatives depicted much higher aryl free radical generation ability. To our delight, the aryl free radical generation of T-Oximer was much stronger (1.08-fold) than that of Con-Oximer, attributing to the larger conjugated T-Oximer with a higher molar extinction coefficient, which could significantly increase the light absorption capability than that of Con-Oximer. Due to the oxygen-independent property of the photolysis reaction of oxime ester, we wonder the aryl free radical generation capacity of T-Oximer NPs under hypoxia conditions. In the hypoxic environment, the absorbance of ABTS+• increased upon the light irradiations, demonstrating that the production of aryl free radical was unaffected (Fig. 3b; Fig. S18, supporting information). Moreover, α-(4-pyridyl N-oxide)-N-tert-butylnitrone (POBN) and N-tert-Butyl-α-phenylnitrone (PBN) were employed as spin traps to capture the released aryl free radical. As shown in Fig. 3c and d, a pronounced electron spin resonance (ESR) signal of aryl free radicals was discernible from oxime ester including T-Oximer NPs and Con-Oximer following LED light irradiation.

The oxime ester can generate alkyl/aryl free radicals in the presence of light, which in turn induces free radical polymerization [6,49,50]. Gelatin methacryloyl (GelMA), photocurable hydrogel, has been widely used for various biomedical applications due to the suitable biological properties and tunable physical characteristics [51–54]. Hence, GelMA was employed as double-bond monomer to explore the ability of T-Oximer NPs to trigger free radical polymerization. Fourier-transform infrared spectroscopy was employed to assess the capacity of

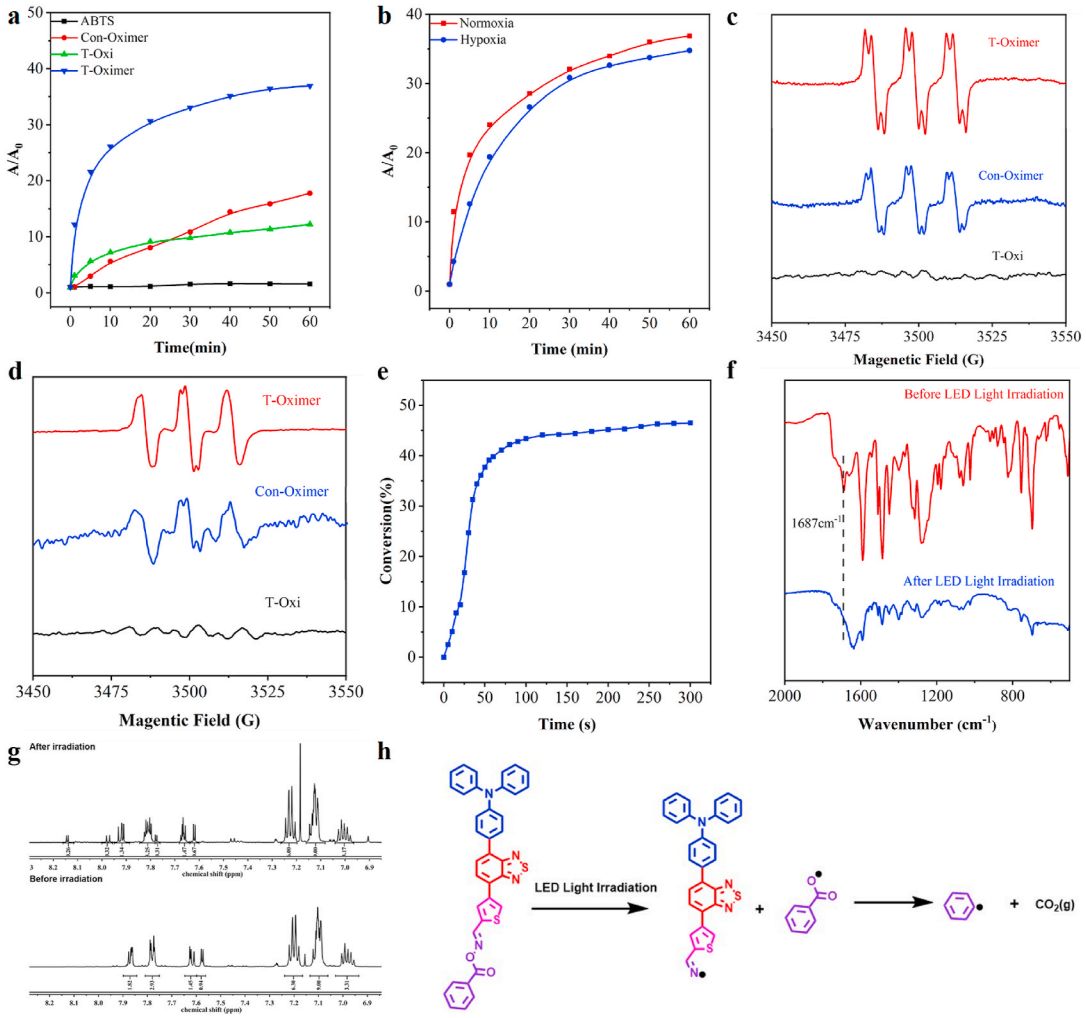

Fig. 3. The generation of aryl free radical *via* photolysis reaction. (a) The absorption enhancement of ABTS (30 μM) at 750 nm in the presence of T-Oximer NPs (10 μM), T-Oxi, and Con-Oximer under LED light irradiation (60 mW/cm^2). (b) The absorption enhancement of ABTS (30 μM) at 750 nm in the presence of T-Oximer NPs (10 μM) under LED light irradiation (60 mW/cm^2) under normoxia and hypoxia conditions. (c) ESR spectra of aryl radical generation from T-Oximer NPs, T-Oxi, and Con-Oximer under LED light irradiation (60 mW/cm^2) tripped by POBN. (d) EPR spectra of aryl radical generation from T-Oximer NPs, T-Oxi, and Con-Oximer under LED light irradiation (60 mW/cm^2) tripped by PBN. (d) Photopolymerization profiles of GelMA initiated by T-Oxime under LED light irradiation (60 mW/cm^2). (f) The IR spectrum of T-Oximer before and after LED light irradiation. (g) The ^{1}H NMR spectrum of T-Oixmer NPs before and after LED irradiation (60 mW/cm^2, 10 min) in $CDCl_3$. (h) Illustration of aryl free radical generation of T-Oximer *via* photolysis reaction.

T-Oximer to facilitate free radical reactions in GelMA after the addition of T-Oximer. The photopolymerization curve of GelMA exhibited a gradual increase in conversion rate over time (Fig. 3e). By adding T-Oximer to the GelMA, the free radical polymerization occurred under white light irradiation to provide corresponding hydrogels (Fig. S19, supporting information). To investigate the photolysis reaction of T-Oximer, a photobleaching test was conducted. As displayed in Fig. S20 (supporting information), the absorbance of T-Oximer diminishes with irradiation, substantiating the hypothesis that T-Oximer underwent photolysis. Moreover, the fluorescent intensity of T-Oximer at approximately 690 nm diminished and a novel fluorescent peak emerged at around 525 nm. T-Oximer was subjected to photolysis, resulting in the fragmentation of the molecule, as evidenced by the IR spectroscopy. The IR spectrum of T-Oximer exhibited a notable disappearance of the peak associated with the oxime ester group following irradiation (Fig. 3f). To gain insight into the photolysis reaction of T-Oximer, ^{1}H NMR spectroscopy analysis before and after LED white light irradiation was further evaluated (Fig. 3g). ^{1}H NMR spectroscopy results of T-Oximer after LED light irradiation revealed the reduction (1.82 vs. 1.34) in the number of H atoms on the benzoyl groups (~7.81 ppm) following irradiation. Moreover, new signals of peak a1 (8.14 ppm), a2 (7.97 ppm), and a3 (7.78 ppm) ascribed to the tertiary methyl hydrogen adjacent of nitrogen radicals and phenyl radical group appeared, respectively, attributing to the break of N-O bond and the release of benzoyl groups (Fig. 3h).

3.4. The DNA bind and DNA cleave effect of T-oximer

Given that oxime ester can bind with DNA and be employed as a photo-induced DNA-cleaving agent, an investigation was conducted into the interaction between T-Oximer and DNA *via* UV–vis and fluorescent spectroscopy. As shown in Fig. 4a, the fluorescence intensity of T-Oximer demonstrates 73.8-fold higher than that of in the absence of DNA. Furthermore, the addition of DNA to T-Oximer increased the absorbance of T-Oximer (Fig. 4b). These findings collectively substantiate the hypothesis that T-Oximer can interact with DNA. Furthermore, an ethidium bromide (EB) displacement experiment was carried out to evaluate possible interactions between T-Oximer and DNA [44]. As exhibited in Fig. 4c, the fluorescence intensity of EB at 590 nm decreased with the increasing concentration of T-Oximer. Conversely, a negligible decrease of EB fluorescence intensity was detected in the presence of T-Oxi (Fig. S21, supporting information). Moreover, 4',

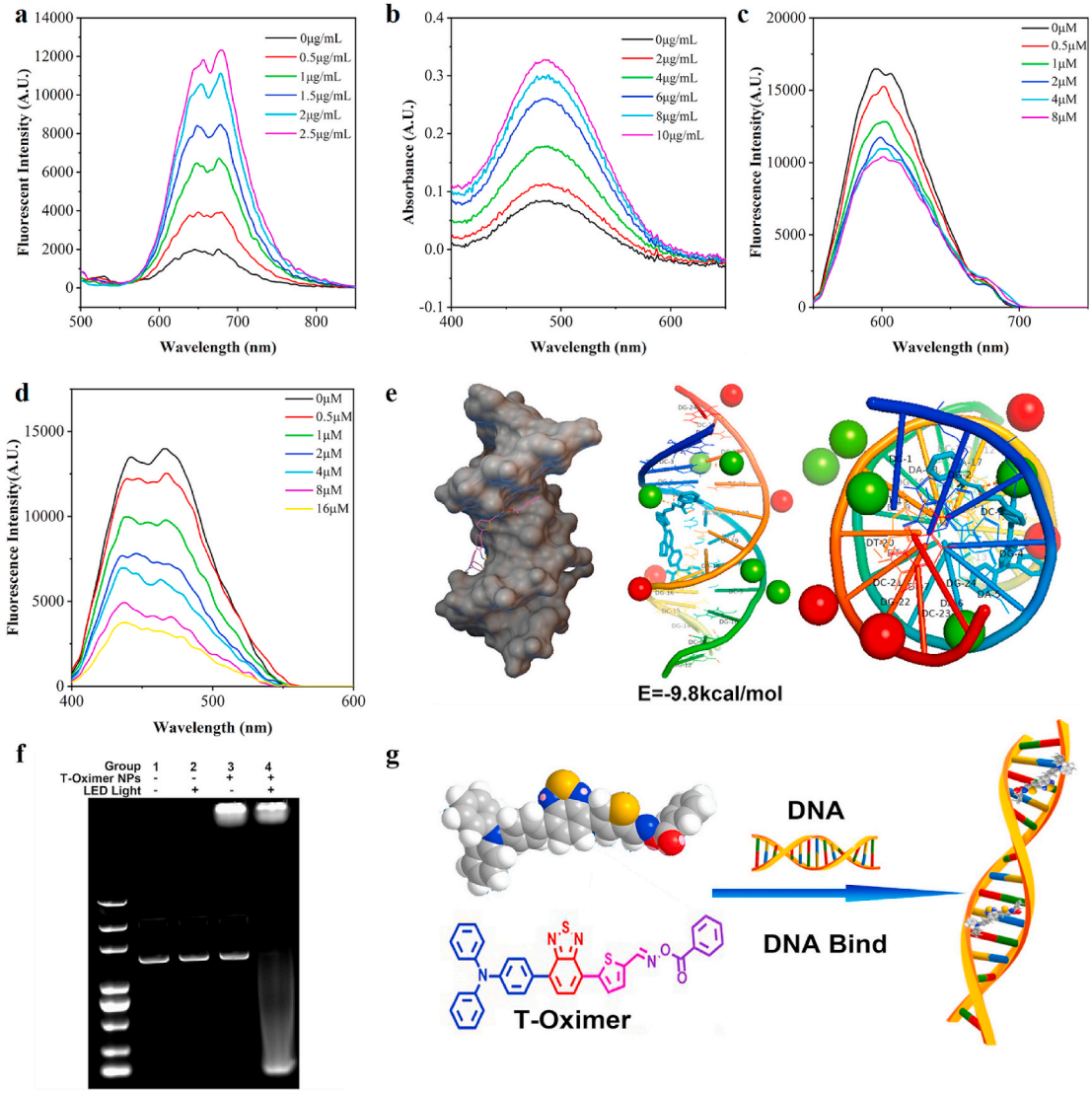

Fig. 4. Binding mode analysis of T-Oximer with DNA. (a) Photoluminescence spectra of DNA solutions with increasing concentrations of the decomposition compounds of T-Oximer. (b) UV–Vis spectra of DNA solutions with increasing concentrations of the decomposition compounds of T-Oximer. (c) Photoluminescence spectra of EB-bonded DNA solutions with increasing concentrations of T-Oximer. (d) Photoluminescence spectra of DAPI-bonded DNA solutions with increasing concentrations of T-Oximer. (e)Molecular docking models of T-Oximer with dsDNA (PDB code: 3u2n). (f) Polyacrylamide gel electrophoresis analysis of DNA with different treatments. (g) Schematic illustration of the binding mode of T-Oximer with DNA.

6-diamidino-2-phenylindole (DAPI) displacement experiments were also carried out to confirm the interaction mode of T-Oximer with DNA. As displayed in Fig. 4d, DAPI fluorescence intensity significantly reduced upon the addition of T-Oximer, while free T-Oxi exhibited a slight reduction of DAPI fluorescence intensity (Fig. S22, supporting information). These results confirmed that T-Oximer could efficiently bind to minor grooves of DNA.

In addition, molecular docking studies show that T-Oximer can insert into small groove of dsDNA with a high docked free energy of −9.8 kcal/mol (Fig. 4e), as multiple hydrogen bonds are formed among the oxygen atom between the oxime ester group and deoxyguanine (dG). By contrast, T-Oxi displays a lower binding free energy of −8.5 kcal/mol (Fig. S23, supporting information). These results further indicate that T-Oximer can interact with DNA *via* groove binding, which is in accordance with the results in DAPI displacement assays. The DNA photocleavage studies of T-Oximer NPs were subjected to investigation through using agarose gel electrophoresis. The analysis of the cleavage products in agarose gel indicated that T-Oximer NPs cleaved DNA and form the nicked pattern, thereby indicating damage to the DNA molecule (Fig. 4f; Fig. S24, supporting information). These findings proved that T-Oximer could bind DNA and cleave DNA upon LED white light irradiation (Fig. 4g).

3.5. *Intracellular superoxide, hydroxyl, and aryl free radicals investigation*

Encouraged by the radical generation capacity of T-Oximer NPs, we continue to investigate the radicals (aryl free radicals and ROS) generation ability of T-Oximer NPs *in vitro* under normoxic or hypoxic conditions (Fig. 5a and b). To evaluate the generation of all radical species within cells, commercial 2′,7′-dichlorodihydrofluorescein diacetate (DCFH-DA) was employed as the probe. In both the normoxic and hypoxic condition, 4T1 cells treated with DCFH-DA after incubation with T-Oximer NPs exhibited obvious fluorescence signals, indicating the production of radicals. Similar positive outcomes in the presence of DHR123 and HPF were observed as well (Fig. 5a and b). Intracellular alkyl/aryl free radicals can trigger the polymerization of monomers with double bonds [45,46]. In particular, the polymerization of the

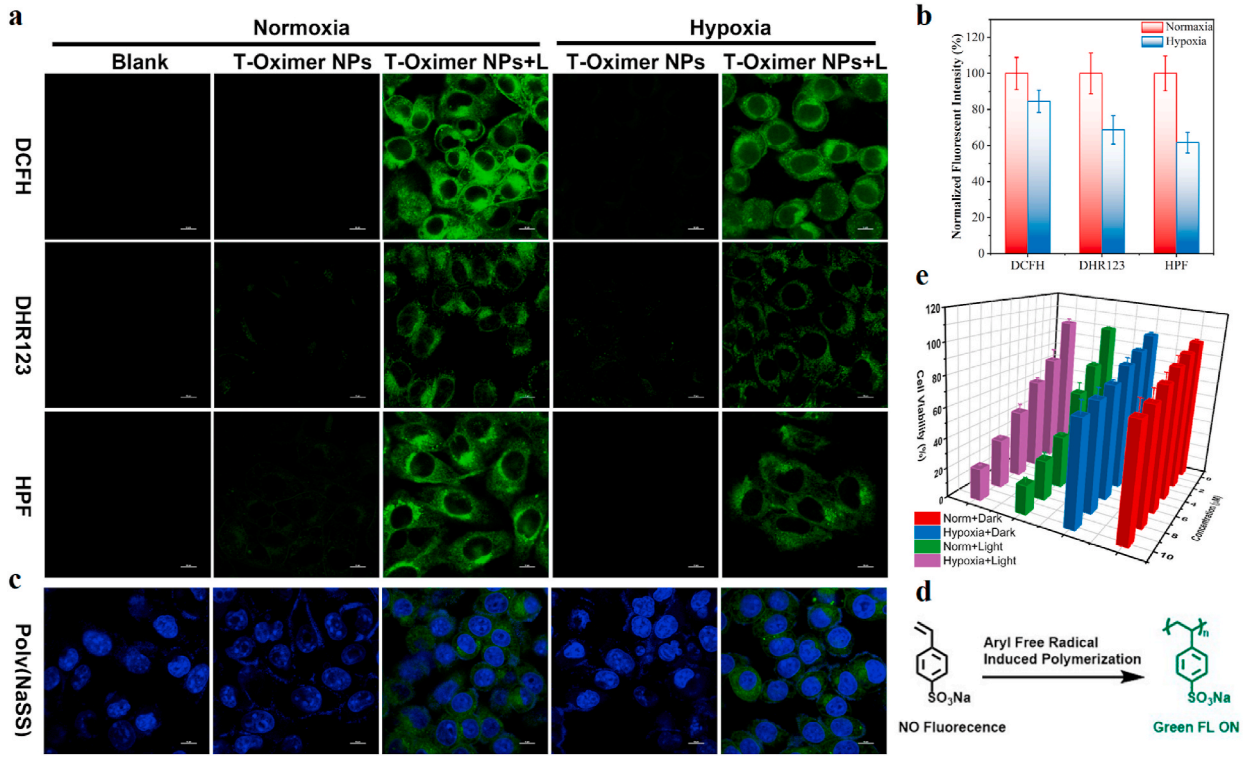

Fig. 5. *In vitro* evaluation on ROS and aryl free radical generation of T-Oximer NPs. (a) Fluorescence imaging of different probes (DCFH, DHR123, and HPF) in the presence of T-Oximer NPs under LED light irradiation in both normoxic and hypoxic conditions. Scale bar = 10 μm. (b) Normalized emission intensity of different probes (DCFH, DHR123, and HPF) in the presence of T-Oximer NPs (5 μM) under LED light irradiation in both normoxic and hypoxic condition. (c) Polymerization of NaSS in cells incubated with T-Oximer NPs under LED light irradiation in both normoxic and hypoxic conditions. The cell nucleus was stained with DAPI (blue), and poly (NaSS) (green). Scale bar = 10 μm. (d) Aryl free radical induced polymerization of NaSS. (e) Cytotoxicity of T-Oximer NPs in the dark and under Light irradiation (60 mW/cm^2, 5 min) on 4T1 cells under normoxic and hypoxic conditions.

4-styrenesulfonate sodium (NaSS) induced the generation of green fluorescence. After irradiation, the bright green fluorescence signal in the cytoplasm was observed, indicated the intracellular production of poly (NaSS) (Fig. 5c). Additionally, the fluorescence of poly (NaSS) was evident in hypoxic cells, demonstrating that T-Oximer NPs can generate aryl free radicals in cells under a hypoxic environment. These findings substantiated the ability of T-Oximer NPs to generate aryl free radicals in both normoxic and hypoxic cells.

Furthermore, the *in vitro* cytotoxicity of T-Oximer NPs under normoxic and hypoxic conditions was investigated using the CCK8 assay. As illustrated in Fig. 5e, the viability of 4T1 cells exceeded 90 % under both normoxic and hypoxic conditions in the absence of irradiation. To our delight, following irradiation (LED, 60 mW/cm^2, 5 min), the viability of 4T1 and MDA-MB-231 cells declined to less than 20 % and less than 25 % in normoxic and hypoxic cells, respectively (Fig. 5e). Moreover, Excellent photodynamic effects were confirmed by the inhibitory concentration 50 % (IC_{50}) of T-Oximer NPs, which was 4.86 μM under normoxic condition and 6.74 μM under hypoxic condition (Fig. S25, supporting information). As a comparison, T-Oxi and Con-Oximer depicted much higher cell viability, indicating outstanding photodynamic effect of T-Oximer NPs (Fig. S26, supporting information).

3.6. Evaluation of cell pyroptosis induced by mitochondrial targeting Type-I ROS and aryl free radical Generator in vitro

Inspired by the ROS and aryl free radical production of T-Oximer NPs *in vitro*, we are prompted to inquire into the subcellular distribution of T-Oximer NPs. Consequently, 4T1 cells were incubated with T-Oximer NPs, and the cellular fluorescence changes were recorded at different time points using confocal laser scanning microscopy (CLSM). T-Oximer NPs were rapidly internalized by cells within 30 min, and the bright fluorescence was still observed after 8 h, confirming the good biocompatibility of T-Oximer NPs (Fig. S27, supporting information). The intracellular distribution of T-Oximer NPs was investigated using commercial organelle-selective trackers (Fig. 6a; Fig. S28, supporting information). In comparison with other probes, the red fluorescence of T-Oximer NPs exhibited a high degree of overlap with the mitochondrial probes of Tracker Green (Pearson's coefficient: 0.947), thereby confirming that T-Oximer NPs were enriched in the mitochondria. To validate the mitochondria-targeting ability attributing to the oxime ester unit, the control CLSM experiments were conducted in which 4T1 cells co-stained with T-Oxi and Con-Oximer. As depicted in Fig. S29 (supporting information), Con-Oximer could target the mitochondria with high Pearson's coefficient up to 0.905. As a comparison, T-Oxi shows poor mitochondria-targeting ability. These results strongly prove that the mitochondria-targeting ability of the oxime ester unit.

MitoSOX immunofluorescence microscopy is a well-established and highly sensitive approach to detect ROS generation in mitochondria. As illustrated in Fig. 6b, the bright green fluorescence signal was observed in the presence of T-Oximer NPs upon light irradiation (LED white light, 60 mW/cm^2, 5 min), suggesting that indicative of elevated mitochondrial ROS levels within the mitochondria of 4T1 cells. Moreover, the control groups exhibited minimal green fluorescence from mitoSOX in 4T1 cells. To evaluate the mitochondrial damaging effect of T-Oximer NPs, Rhod 123 was selected as an indicator to investigate the mitochondrial membrane potential (MMP) level of 4T1 cells. As shown in Fig. 6c, the green fluorescence from Rhod 123 was drastically quenched in the 4T1 cells incubation with T-Oximer NPs upon LED white light irradiation, verifying the depolarization of MMP and mitochondria damage. The generation of excessive amounts of ROS in mitochondria has been demonstrated to enhance DNA damage in tumor cells by oxidizing nucleoside bases, thereby impairing the physiological

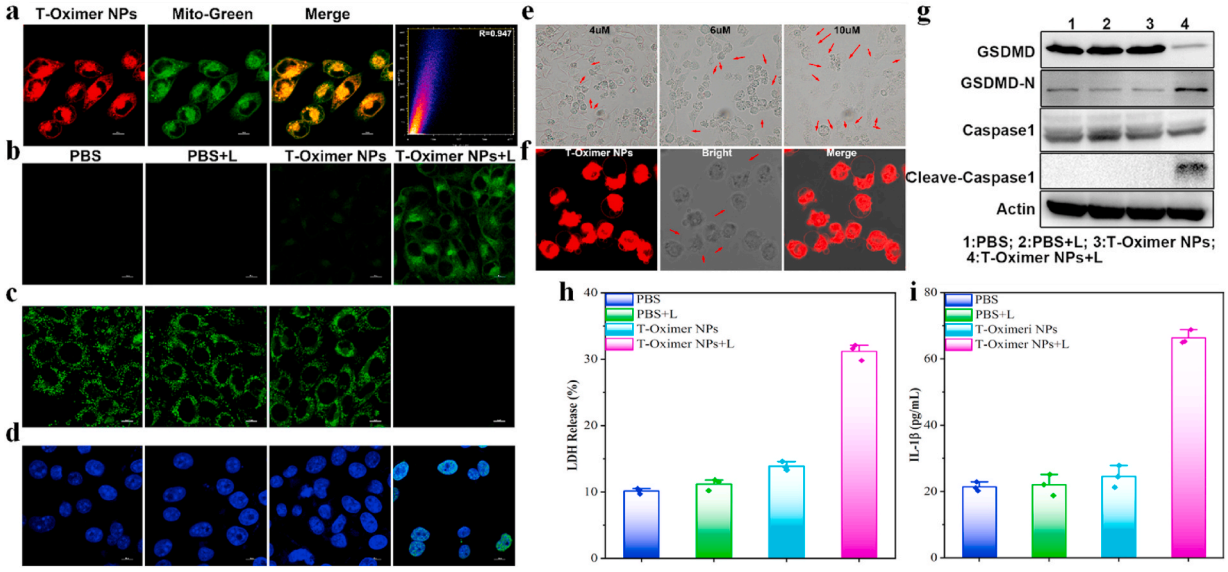

Fig. 6. *In vitro* study on T-Oximer NPs -mediated cell death mechanism. (a) The colocation of T-Oximer NPs (in red) with Mito-tracker green (in green) in 4T1 cells. Scale bar = 10 μm. (b) CLSM images of mitochondrial ROS generated in 4T1 cells using mitoSOX as an indicator after different treatments. Scale bar = 10 μm. (c) CLSM images of mitochondrial membrane potential using Rhod123 as an indicator in 4T1 cells after various treatments. Scale bar = 10 μm. (d) γH2AX immunofluorescence in 4T1 cells with different treatments. Scale bar = 10 μm. (e)Representative phase-contrast images of the typical pyroptotic bubbling mediated by T-Oximer NPs-mediated mitochondrial targeting type-I PDT/photolysis. Pyroptotic cells are indicated by the red arrows. (f) Representative CLSM images of the typical pyroptotic bubbling mediated by T-Oximer NPs-mediated mitochondrial targeting type-I PDT/photolysis. (g) The expression of the pyroptosis-associated proteins (i.e., GSDMD, GSDMD-N, Caspase-1, and cleaved Caspasse-1) in 4T1 cells was analyzed using WB. The levels of released LDH (h), and IL-1β(i) in cell culture media after various treatments.

functions of tumor cells. The use of γH2AX immuno-fluorescence microscopy represents a well-accepted and sensitive method for the detection of DNA damage. As illustrated in Fig. 6d, a notable green γH2AX fluorescence signal inside 4T1 cell nucleus was appeared in the presence of T-Oximer NPs after irradiation (LED light, 60 mW/cm^2, 5 min), indicating the phenomenon of DNA damage. Conversely, no discernible DNA damage was observed in the control groups. Herein, these results prove that T-Oximer NPs can damage cellular DNA through the photolysis reaction of oxime ester.

Pyroptosis, a proinflammatory form of programmed cell death (PCD), has the potential to enhance anticancer immunity. It has been proposed that PDT-mediated mitochondrial ROS generation and DNA cleavage may serve as a trigger for tumor cell pyroptosis. Specifically, elevated levels of mitochondrial ROS or aryl free radical have the potential to damage mitochondria, cleave DNA, and enhance the caspase-1 expression, which subsequently cleaves GSDMD and produce the GSDMD-N domain, resulting in membrane perforation and the execution of pyroptosis [55,56]. In light of these insights, we put forth the hypothesis that the generation of type-I ROS and aryl free radicals in mitochondria *in situ* could serve as an efficient means of amplifying pyroptosis induction in tumor cells. During pyroptosis, cells carry out rapid plasma membrane rupture and swiftly release proinflammatory mediators and immunogenic materials, inducing the activation and infiltration of immune cells. Consequently, the morphology of tumor cells subjected to different treatments was monitored *via* phase contrast microscopy and CLFM. As illustrated in Fig. 6e and f, the hallmarks of pyroptosis, including cell swelling and the formation of bubbles from the plasma membrane, were observed in the cells after T-Oximer NPs + L treatment. Moreover, the cells incubated with T-Oximer NPs alone demonstrated some pyroptotic characteristics. In comparison, negligible morphological changes were observed in the other group. Furthermore, the pyroptosis progression in 4T1 cells incubated with T-Oximer NPs upon LED white light irradiation was investigated. Following light exposure, pyroptosis occurred around 4 h after PDT/photolysis treatment, with the cells tending to burst at 8 h (Fig. S30, supporting information). All these results verify the hypothesis that the T-Oximer NPs can evoke pyroptosis. Western blotting was employed to analyze the expression of pyroptosis-corresponding proteins in 4T1 cells. It is noteworthy that a considerable increase in the expression of cleaved GSDMD-N was observed in the T-Oximer NPs + L group (Fig. 6g; Fig. S31, supporting information). The augmented GSDMD-N concentration in the T-Oximer NPs + L cohort, in comparison to the T-Oximer NPs monotherapy, underscored the pivotal role of mitochondrial-targeting type-I PDT/photolysis in the induction of pyroptosis. This elevation of GSDMD-N was associated with the upregulation of cleaved caspase-1 expression. The enhancement in cleaved caspase-1 expression was detected in the T-Oximer NPs + L groups. Subsequently, the lactate dehydrogenase (LDH) assay kit and enzyme-linked immunosorbent assay (ELISA) analysis of 4T1 cell supernatant demonstrated that the liberation of LDH and IL-1β in T-Oximer NPs + L group exhibited an increase in comparison to those in other groups (Fig. 6h and i). These findings substantiate the hypothesis that the production of type-I ROS and aryl free radicals in mitochondria *in situ* based on T-Oximer NPs can induce the destruction of cell membranes, release cellular contents, and trigger pyroptosis.

3.7. The ICD effect of pyroptosis in vitro

The effective induction of pyroptosis provides an approach to activate immune responses. Therefore, we proceeded to explore the immunogenicity marker of tumor cells such as high-mobility group box 1 (HMGB1) and exposure to calreticulin (CRT). As displayed in Fig. 7a and b, a notable translocation of HMGB1 from the nuclei to the extracellular space was observed, as well as the exposure of CRT on the cell membrane was detected. The enhanced release of HMGB1 in the cell supernatant from the T-Oximer NPs + L-treated 4T1 cells was consistent with the CLSM results (Fig. 7c). The 4T1 cells treated with T-Oximer NPs + L demonstrated a notable release of adenosine triphosphate (ATP) in the cell supernatant, with the released ATP in the T-Oximer NPs + L group being 4.68-fold higher than that in the PBS group (Fig. 7d). Additionally, the ELISA supernatant revealed the release of interleukin-6 (IL-6) and tumor necrosis factor-α (TNF-α), which are pro-inflammatory

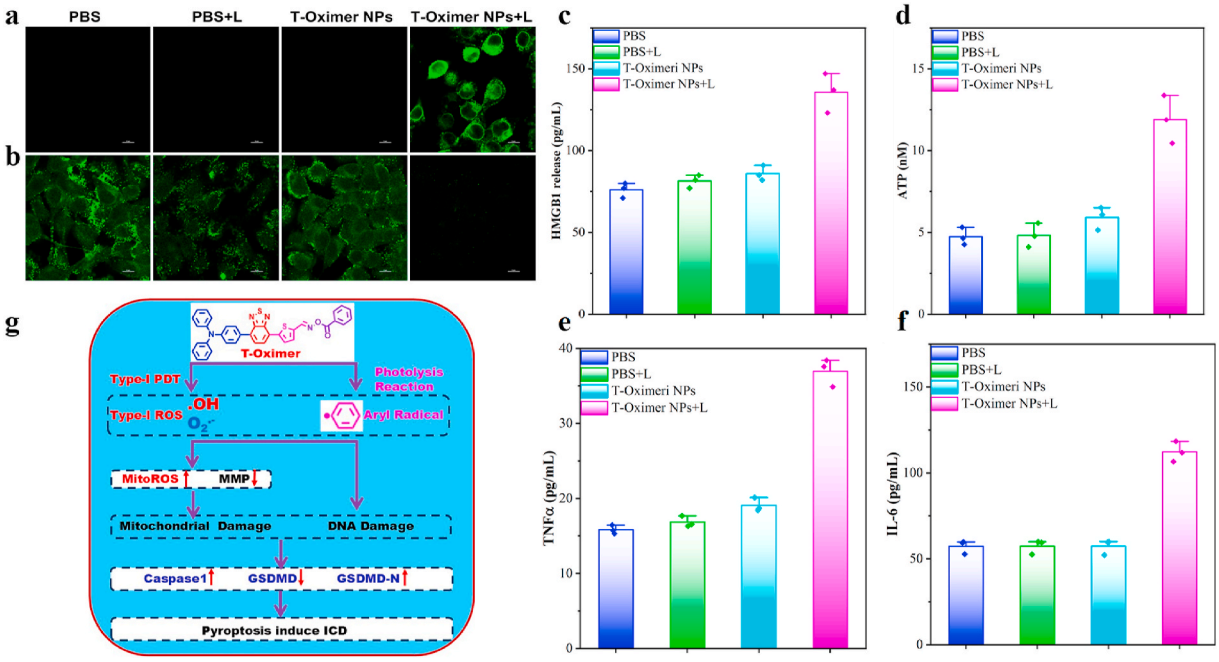

Fig. 7. *In vitro* study on T-Oximer NPs -mediated ICD effect. (a) CLSM images of CRT expression in 4T1 cells after various treatments. Scale bar = 10 μm. (b) CLSM images of HMGB1 expression in 4T1 cells after various treatments. Scale bar = 10 μm. The levels of released HMGB1(c), ATP(d), TNFα (e), and IL-6 (f) in cell culture media after various treatments. (g) Schematic illustration of the process of pyroptosis induced by T-Oximer NPs under LED Light irradiation.

cytokines. Following treatment with T-Oximer NPs + L, greater levels of TNF-α and IL-6 secretion were observed in comparison to the control groups (Fig. 7e and f). These findings validate the pyroptosis-mediated ICD effect of mitochondrial targeting type-I PDT/photolysis based on T-Oximer NPs (Fig. 7g).

3.8. The in vivo NIR fluorescent imaging

The distribution behavior of T-Oximer NPs was evaluated following intravenous administration. T-Oximer NPs were administered intravenously into 4T1 tumor-bearing mice, and NIR fluorescent imaging was then carried out using IVIS. As illustrated in Fig. S32 (supporting information), NIR fluorescence signals at tumor tissues were observed, reaching a maximum at approximately 24 h post-injection. In light of this favorable tumor-targeting enrichment behavior, tumors were irradiated by white light at 24 h post-injection for treatment. It is noteworthy that even at 48 h post-injection, the NIR fluorescence at the tumor site would be detected, indicating the intratumoral retention of T-Oximer NPs. At 24 h post-intravenous injection, major organs (spleen, heart, kidneys, liver, and lung) and the tumor were collected and performed for *ex vivo* imaging (Fig. S33, supporting information). The elevated NIR fluorescent signal of T-Oximer NPs in tumor tissue, in comparison to the liver, can be attributed to the effective accumulation in the tumor.

3.9. Therapeutic effects in vivo

Subsequently, the antitumor therapeutic efficacy of T-Oximer NPs was evaluated in 4T1 tumor-bearing BALB/c mice. The mice were randomly assigned to four groups (n = 4 mice per group) and subjected to a series of treatments. The experimental groups were as follows: PBS, PBS + L, T-Oximer NPs, and T-Oximer NPs + L. In the groups marked with "L", the tumor sites were irradiated for 15 min by LED white light (60 mW/cm^2) after 24 h post-injection. The timeline for the treatment of the tumor is illustrated in Fig. 8a. Tumor growth and body weight were monitored on a biweekly basis. The T-Oximer NPs group demonstrated a modest inhibitory effect on tumor growth, compared with the PBS and light groups. Moreover, T-Oximer NPs + L group displayed a more pronounced antitumor effect in comparison to the other groups (Fig. 8b and c). For example, the mean tumor volume in the 'T-Oximer NPs + L' group exhibited a reduction throughout the course of the treatment. Additionally, the mean tumor volume in the T-Oximer NPs + L group on day 14 was observed to be smaller than that of the other groups. Moreover, the weight of the excised tumor on day 14 verified the superior antitumor efficacy of the T-Oximer NPs + L treatment in comparison to the other interventions (Fig. 8d). Furthermore, all lungs were collected for histological examination using hematoxylin and eosin (H&E) staining, with the objective of evaluating the type-I PDT/photolysis-induced anti-metastatic effect. The number of lung metastatic nodules exhibited a marked decline in the T-Oximer NPs + L group, whereas discernible tumor metastases were observed in the lungs of the other groups (Fig. 8e). The quantification of metastatic foci coverage on lungs also demonstrated that the T-Oximer NPs + L group exhibited the most pronounced anti-metastasis effect (Fig. 8f). These findings illustrate that mitochondrial-targeting type-I PDT/photolysis can not only effectively inhibit tumor growth but also evoke systemic antitumor immunity *via* pyroptosis induction, thereby suppressing tumor growth and metastasis. No significant variations in the body weights of mice in the therapeutic groups were observed in comparison to the control group during the treatment period (Fig. 8g), indicating that T-Oximer NPs possess excellent biocompatibility.

The levels of ROS in tumor tissues were subsequently assessed through immunofluorescence staining. The generation of ROS in the intratumoral region following type-I PDT/photolysis was investigated in a series of groups, including the PBS, PBS + L, T-Oximer NPs, and T-Oximer NPs + L groups, on day 2 using DCFH-DA. Green DCF fluorescence was observed exclusively in the tumor tissues of the T-Oximer NPs + L group, which confirmed the potent type-I PDT/photolysis effect mediated by the T-Oximer NPs (Fig. S34, supporting information). To evaluate the extent of pyroptosis and necrosis in tumor tissues after various treatments, histological staining (H&E and TUNEL staining) was performed. Histological examination revealed that the PBS group exhibited severe histological damage to tumor cells compared to the T-Oximer NPs + L group (Fig. S35, supporting information). Furthermore,

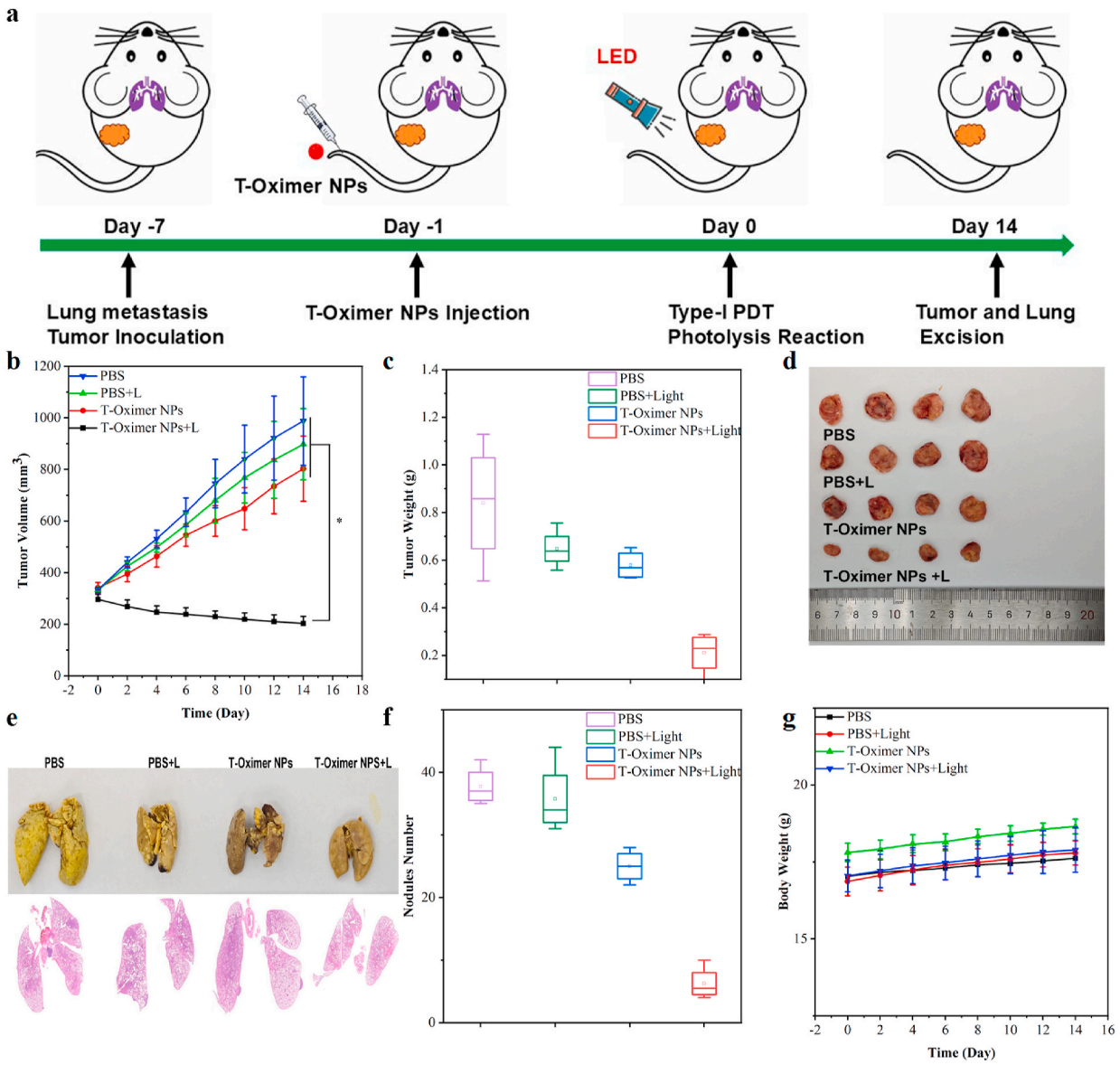

Fig. 8. The anti-tumor and anti-metastasis therapeutic evaluation of mitochondrial-targeting type-I PDT/photolysis. (a)The time pipe of anti-tumor and anti-metastasis therapy. (b) The tumor volume curving of 4T1-bearing mice after different treatments. (c) The tumor weight of 4T1-bearing mice after different treatments. (d) The photography of tumor tissues after different treatments. (e) The photos of lungs and H&E staining lung tissues after different treatments. (f) The metastasis nodules number in lung tissues after different treatments. (g) Changes in body weight of the 4T1-bearing mice after different treatments.

the T-Oximer NPs + L treatment enhanced the green fluorescence in TUNEL staining (Fig. S36, supporting information), suggesting higher cell apoptosis and necrosis. All these results confirmed that pyroptosis and necrosis were observed in the T-Oximer NPs + L group, which aligned with the potent tumor inhibition effect.

3.10. The mechanism of anti-tumor effect

To determine whether the pyroptosis induced by the mitochondrial-targeted type-I PDT could enhance the systemic immune response, we carried out immunological analyses to elucidate the underlying mechanisms. DCs, tumor-infiltrated immune cells, and tumor-associated macrophages (TAMs) in tumor tissues as well as related cytokines in serum were explored after different treatments. As anticipated, T-Oximer NPs were observed to effectively induce DC maturation upon whit light irradiation, with the number of mature DCs increasing by a factor of 1.36 in comparison to the PBS group (Fig. 9a). To further substantiate the immunotherapeutic efficacy of mitochondrial-targeted type-I PDT/photolysis based on T-Oximer NPs, the infiltration of T cells following various treatments within the tumor was also investigated. The proportion of $CD8^+$ T cells in the tumor was 6.3 % following treatment with T-Oximer NPs + L, which was 2.25-fold that observed in the PBS group (Fig. 9b). Furthermore, the proportion of $CD4^+$ T cells was also enhanced after T-Oximer NPs + L treatment, which was 3.09-fold higher than that of the PBS groups (Fig. 9b). These findings collectively indicate that the mitochondrial-targeted type-I PDT/photolysis based on the T-Oximer NPs can enhance the activation and maturation of DC, improve the infiltration of T cells, and trigger an immune response.

Previous studies have demonstrated that pyropotisis could reverse the tumor's immune microenvironment. In addition, the expression of tumor-associated macrophage (TAM) in the tumor tissues was also investigated. Firstly, the abundance of TAMs in tumor tissues following different treatments was exploited using flow cytometry. As illustrated in Fig. 9c, the lowest proportion of $CD206^+$ $CD163^+$ cells was observed in the T-Oximer NPs + L group (17.0 %), which was lower than that

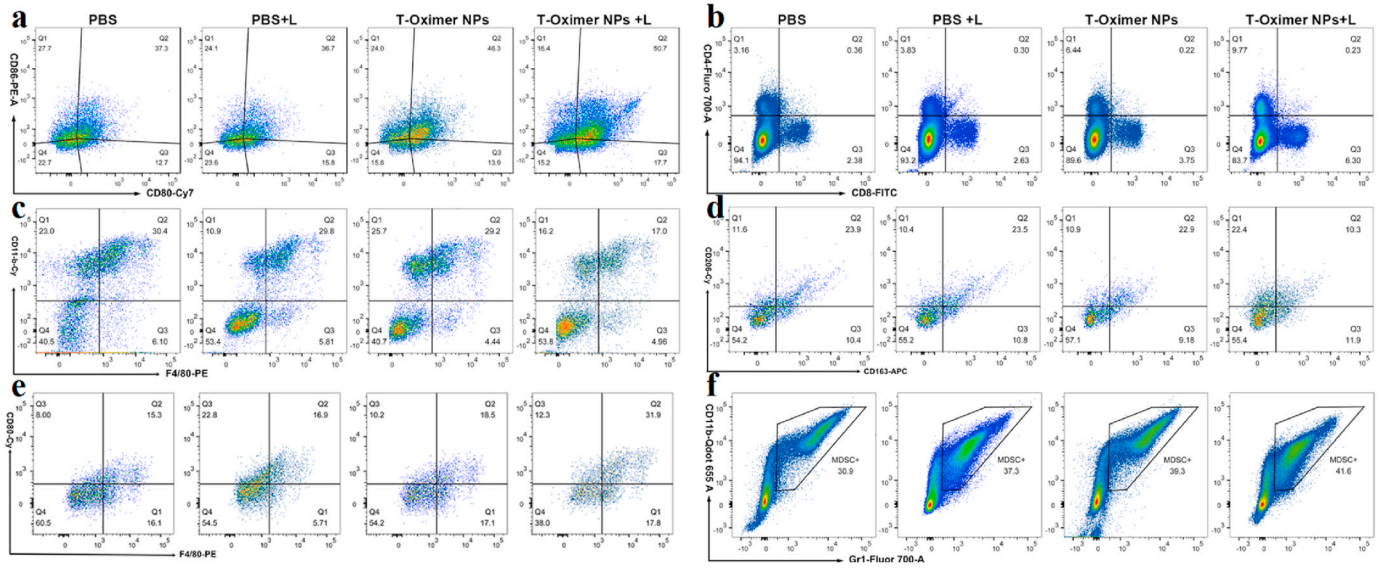

Fig. 9. *In vivo* immune responses induced by T-Oximer NPs based mitochondrial-targeting type-I PDT/photolysis. (a) DC maturation markers ($CD80^+$ $CD86^+$). (b) $CD4^+$ $CD8^+$ T cell proportions. (c) The TAM (CD11b + F4/80+) proportions. (d) M2-like phenotype macrophages (CD163+ CD206 cells) proportions. (e) M1-like phenotype macrophages ($CD80^+$ F4/80+cells) proportions. (f) The proportions of Gr-1+CD11b + cells among tumor-infiltrating $CD45^+$ cells.

observed in the PBS group (30.4 %), the PBS + L group (29.8 %), and the T-Oximer NPs group (29.2 %). These findings confirm that mitochondrial-targeting type-I PDT/photolysis is the most effective method for reducing the number of TAMs, thereby enhancing anti-tumor immunotherapy. It is noteworthy that mitochondrial-targeting type-I PDT/photolysis treatment resulted in a notable decrease in the proportion of anti-inflammatory M2 macrophages, while the number of pro-inflammatory M1 macrophages significantly increased (Fig. 9d and e). This suggests that mitochondrial-targeting type-I PDT/photolysis reversed the polarization of TAMs from the anti-inflammatory M2 phenotype to the pro-inflammatory M1 phenotype. Apart from that, the macrophages in tumor tissues were also evaluated. The results showed that the relative proportion of M1 macrophages (F4/80+ $CD80^+$) increased from 15.3 % to 31.9 % treated by T-Oximer NPs + L, and the M2 macrophages (F4/80+ CD206+) decreased from 23.9 % to 10.3 %. Notably, T-Oximer NPs + L significantly promoted the polarization of M2 type macrophages to M1 type, resulting in a M1/M2 ratio (3.09) significantly higher than that in other treatment groups. These findings substantiate that T-Oximer NPs + L can deplete TAM, reduce suppressor cells, decrease the percentage of M2-like macrophages, and reverse the immunosuppressive microenvironment. Moreover, the alterations in immunosuppressive immune cells, MDSC+, were also evaluated. As illustrated in Fig. 9f, T-Oximer NPs + L treatment effectively diminished the number of MDSC+. As depicted in Fig. S37 (supporting information), there was a 0.66-fold decline in CD + Tregs after mitochondrial-targeting type-I PDT/photolysis treatment compared to PBS group. The change of Tregs values after PDT, indicating the anti-tumor immunity effect of T-Oximer NPs. These findings substantiate that T-Oximer NPs + L can deplete TAM, reduce suppressor cells, decrease the percentage of M2-like macrophages, and reverse the immunosuppressive microenvironment.

Finally, the serum levels of immune-relevant inflammatory cytokines, including TNFα, IL-6, IL-1β, and IFN-γ, were detected. As depicted in Fig. S38 (supporting information), the level of these cytokines was significantly elevated in the T-Oximer NPs + L group in comparison to the other groups till to 72 h, thereby verifying the activation of cancer cell pyroptosis by the immune system. Furthermore, T-Oximer NPs-mediated mitochondrial targeting type-I PDT/photolysis effectively facilitated the infiltration of immune cells and reversed the immunesuppressive tumor microenvironment, thereby triggering great interest in the treatment of more aggressive and metastatic tumors.

3.11. *The abscopal effect boosted by mitochondrial targeting Type-I PDT/photolysis based on T-oximer NPs*

The photodynamic enhanced pyroptosis based on T-Oximer NPs has been demonstrated to induce the suppression of distant tumors as a result of the activation of systemic immunity. The *in vivo* efficacy of mitochondrial-targeting type-I PDT/photolysis and the abscopal effects of T-Oximer NPs-based pyroptosis-mediated photoimmunotherapy were further evaluated using a bilateral 4T1 tumor-bearing mouse model (Fig. 10a). Tumor volumes and body weights were monitored on a biweekly basis for a period of 14 days. As with the preceding results, the growth of the primary tumor was inhibited following treatment with T-Oximer NPs + L. This may be attributed to the alleviation of the immunosuppressive microenvironment and the enhancement of T cell infiltration (Fig. 10b-10d). As anticipated, the T-Oximer NPs + L group exhibited discernible abscopal effects, evidenced by a delayed growth of distant tumors (Fig. 10e and f). The representative tumor photographs also displayed a notable regression of the untreated distant tumor, which suggests that the localized mitochondrial-targeting type-I PDT/photolysis has activated systemic antitumor immune responses (Fig. 10g). Furthermore, the body weights of all mice remained stable throughout the course of treatment, indicating minimal systemic toxicity (Fig. S39, supporting information). Collectively, these results suggest that the T-Oximer NPs-based pyroptosis-mediated photoimmunotherapy can evoke a robust systemic immune response to inhibit the growth of both primary and distant tumors.

3.12. *Biosafe*

Finally, the *in vivo* biosafety of T-Oximer NPs was ultimately assessed. Healthy BALB/c mice were administered intravenous injections of T-Oximer NPs on days 0, 3, 6, and 9. On day 16, the major organs (kidneys, heart, spleen, liver, and lung) were collected for H&E staining. The mice treated with T-Oximer NPs demonstrated no discernible histological abnormalities in the major organs (Fig. S40, supporting information). Moreover, serum biochemistry studies were undertaken to investigate liver and renal function biomarkers, such as albumin (ALB), blood urea nitrogen (BUN), aspartate transaminase (AST), alkaline phosphatase (ALP), creatine kinase (CK), alanine transaminase (ALT), uric acid (UA), and creatinine (CR). All the parameters fall within the respective normal range (Fig. S41, supporting

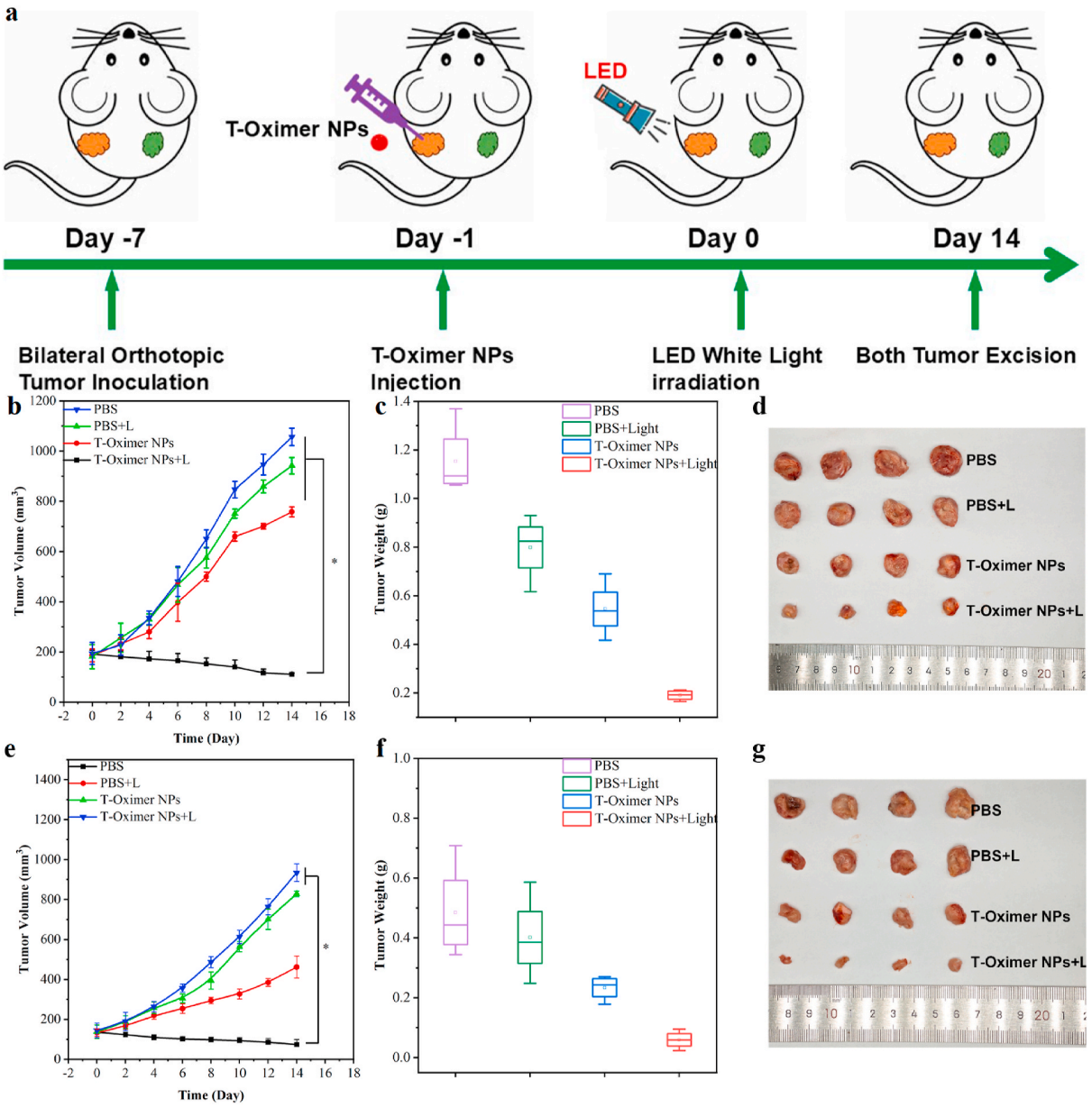

Fig. 10. The abscopal effect of T-Oximer NPs-based pyroptosis-mediated photoimmunotherapy. (a) Schematic illustration of abscopal effect therapy. (b) The primary tumor growth curving of mice after different treatments. (c) The primary tumor weight of mice after different treatments. (d) The photograph of primary tumor tissues after different treatments. (e) The distant tumor growth curving of mice after different treatments. (f) The distant tumor weight of mice after different treatments. (g) The photograph of distant tumor tissues after different treatments.

information), demonstrating the absence of liver or kidney dysfunction. All these findings verified the high biocompatibility of T-Oximer NPs.

4. Conclusions

In summary, the first example of type-I ROS/aryl free radicals combined photogenerator (visible light-active oxime ester, T-Oximer), which can produce type-I ROS ($O_2^{\bullet-}$ and •OH) *via* type-I electron transfer process and generate aryl free radicals through photolysis reaction, has been successfully developed for oxygen-independent pyroptosis-mediated photoimmunotherapy against hypoxic tumors. Another unexpected property of T-Oximer is its efficient accumulation in mitochondria, which can enhance mitochondrial radical levels, and damage mitochondria in hypoxic tumor cells. Apart from that, the particularly DNA binding and cleaving feature of T-Oximer can significantly enhance the efficacy of DNA damage. Leveraging the multiple properties including boosting combined type-I ROS/aryl free radicals, targeting and damaging mitochondria, DNA binding and cleavage, T-Oximer can trigger pyroptosis, enhance the ICD effect, and induce potent systemic antitumor immunity to inhibit tumor growth and suppress metastasis. In conclusion, our study provides new insights into the treatment of hypoxic solid tumors and promotes the clinical application of oxygen-independent pyroptosis-mediated photoimmunotherapy based on type-I ROS/aryl free radicals combined photogenerator.

CRediT authorship contribution statement

Qiyu Zhan: Writing – original draft, Investigation, Formal analysis, Data curation. **Yulin Kuang:** Writing – original draft, Investigation, Formal analysis. **Xuyuan Chen:** Writing – original draft, Investigation, Formal analysis. **Yanzhen Yang:** Formal analysis, Investigation, Writing – original draft. **Linhui Jiang:** Formal analysis, Investigation, Writing –

original draft. **Jian Chen:** Writing – original draft, Investigation, Formal analysis. **Lie Li:** Writing – original draft, Investigation, Formal analysis. **Junwei Wang:** Writing – original draft, Investigation, Formal analysis. **Shuoji Zhu:** Writing – review & editing, Writing – original draft, Project administration, Investigation, Formal analysis, Data curation, Conceptualization. **Huanlei Huang:** Writing – review & editing, Writing – original draft, Project administration, Investigation, Formal analysis, Data curation, Conceptualization. **Lei Wang:** Writing – review & editing, Writing – original draft, Project administration, Investigation, Funding acquisition, Formal analysis, Data curation, Conceptualization. **Ping Zhu:** Writing – review & editing, Writing – original draft, Project administration, Investigation, Funding acquisition, Formal analysis, Data curation, Conceptualization. **Ruiyuan Liu:** Writing – review & editing, Writing – original draft, Supervision, Project administration, Funding acquisition, Conceptualization.

Ethics approval and consent to participate

Animal experiments were conducted with approval from the Ethical Committee of Animal Experiments of South Medical University (SCXK 2016–0041) and according to the Committee Guidelines.

Declaration of competing interest

The authors declare that they have no known competing financial interests or personal relationships that could have appeared to influence the work reported in this paper.

Acknowledgements

This work was partially funded by the National Natural Science Foundation of China (No. 22308192), the Guangdong Provincial Special Support Program for Prominent Talents (2021JC06Y656), the Natural Science Foundation of Guangdong Province, China (No. 2023A1515012934), and Guangdong Province Marine Economic Development Project (No. GDNRC[2024]27).

Appendix A. Supplementary data

Supplementary data to this article can be found online at https://doi.org/10.1016/j.bioactmat.2025.01.032.

References

[1] C. Zhu, S. Xu, R. Jiang, et al., The gasdermin family: emerging therapeutic targets in diseases, Signal. Transduct. Tar. 9 (1) (2024) 87.
[2] L. Lu, Y. Zhang, X. Tan, et al., Emerging mechanisms of pyroptosis and its therapeutic strategy in cancer, Cell Death Dis. 8 (1) (2022) 338.
[3] P. Yu, X. Zhang, N. Liu, et al., Pyroptosis: mechanisms and diseases, Signal. Transduct. Tar. 6 (1) (2021) 128.
[4] S. Zeng, C. Chen, L. Zhang, et al., Activation of pyroptosis by specific organelle-targeting photodynamic therapy to amplify immunogenic cell death for anti-tumor immunotherapy, Bioact. Mater. 25 (2023) 580–593.
[5] W. Qin, L. Qiao, Q. Wang, et al., Advancing precision: a controllable self-synergistic nanoplatform initiating pyroptosis-based immunogenic cell death cascade for targeted tumor therapy, ACS Nano 18 (2) (2024) 1582–1598.
[6] B. Ding, H. Chen, J. Tan, et al., ZIF-8 nanoparticles evoke pyroptosis for high-efficiency cancer immunotherapy, Angew. Chem., Int. Ed. 62 (10) (2023) e202215307.
[7] M.-J. Zhang, Y.-Y. Wang, L.-L. Han, et al., Biomaterials elicit pyroptosis enhancing cancer immunotherapy, Adv. Funct. Mater. 34 (7) (2024) 2311362.
[8] M. Li, J. Kim, H. Rha, et al., Photon-controlled pyroptosis activation (photopyro): an emerging trigger for antitumor immune response, J. Am. Chem. Soc. 145 (11) (2023) 6007–6023.
[9] W. Gao, X. Wang, Y. Zhou, et al., Autophagy, ferroptosis, pyroptosis, and necroptosis in tumor immunotherapy, Signal. Transduct. Tar. 7 (1) (2022) 196.
[10] X. Li, J.F. Lovell, J. Yoon, et al., Clinical development and potential of photothermal and photodynamic therapies for cancer, Nat. Rev. Clin. Oncol. 17 (11) (2020) 657–674.
[11] D.E. Dolmans, D. Fukumura, R.K. Jain, Photodynamic therapy for cancer, Nat. Rev. Cancer 3 (5) (2003) 380–387.
[12] J.P. Celli, B.Q. Spring, I. Rizvi, et al., Imaging and photodynamic therapy: mechanisms, monitoring, and optimization, Chem. Rev. 110 (5) (2010) 2795–2838.
[13] T.C. Pham, V.N. Nguyen, Y. Choi, et al., Recent strategies to develop innovative photosensitizers for enhanced photodynamic therapy, Chem. Rev. 121 (21) (2021) 13454–13619.
[14] X. Zhao, J. Liu, J. Fan, et al., Recent progress in photosensitizers for overcoming the challenges of photodynamic therapy: from molecular design to application, Chem. Soc. Rev. 50 (6) (2021) 4185–4219.
[15] S.S. Lucky, K.C. Soo, Y. Zhang, Nanoparticles in photodynamic therapy, Chem. Rev. 115 (4) (2015) 1990–2042.
[16] J. Chen, T. Fan, Z. Xie, et al., Advances in nanomaterials for photodynamic therapy applications: status and challenges, Biomaterials 237 (2020) 119827.
[17] Y.-Y. Wang, Y.-C. Liu, H. Sun, et al., Type I photodynamic therapy by organic-inorganic hybrid materials: from strategies to applications, Coord. Chem. Rev. 395 (2019) 46–62.
[18] W. Fan, P. Huang, X. Chen, Overcoming the Achilles' heel of photodynamic therapy, Chem. Soc. Rev. 45 (23) (2016) 6488–6519.
[19] J. Du, T. Shi, S. Long, et al., Enhanced photodynamic therapy for overcoming tumor hypoxia: from microenvironment regulation to photosensitizer innovation, Coord. Chem. Rev. 427 (2021) 213604.
[20] J. Xing, Y. Yang, W. Zhang, et al., Injectable hydrogel containing TiO nanosheets for synergistic photothermal/thermodynamic therapy, ACS Appl. Mater. Interfaces 15 (29) (2023) 34436–34450.
[21] K.W. Lee, Y. Wan, X. Li, et al., Recent progress of alkyl radicals generation-based agents for biomedical applications, Adv. Healthcare Mater. 10 (10) (2021) e2100055.
[22] H. Li, K. Yang, L. Hai, et al., Photothermal-triggered release of alkyl radicals and cascade generation of hydroxyl radicals via a versatile hybrid nanocatalyst for hypoxia-irrelevant synergistic antibiofilm therapy, Chem. Eng. J. 455 (2023) 140903.
[23] Y. Dai, H. Zhao, K. He, et al., NIR-II excitation phototheranostic nanomedicine for fluorescence/photoacoustic tumor imaging and targeted photothermal-photonic thermodynamic therapy, Small 17 (42) (2021) e2102527.
[24] Y.-H. Wu, B. Graff, J. Lalevée, et al., Visible light-induced free radical polymerization utilizing halogen-containing triphenylamine oxime esters as Type I photoinitiators, Eur. Polym. J. 217 (2024) 113300.
[25] X. Sun, M. Jin, X. Wu, et al., Bis-substituted thiophene-containing oxime sulfonates photoacid generators for cationic polymerization under UV-visible LED irradiation, J. Polym. Sci. Poly. Chem. 56 (7) (2018) 776–782.
[26] D.E. Fast, A. Lauer, J.P. Menzel, et al., Wavelength-dependent photochemistry of oxime ester photoinitiators, Macromolecules 50 (5) (2017) 1815–1823.
[27] H. Song, Y. Liu, L. Xiong, et al., Design, synthesis, and insecticidal evaluation of new pyrazole derivatives containing imine, oxime ether, oxime ester, and dihydroisoxazoline groups based on the inhibitor binding pocket of respiratory complex I, J. Agric. Food Chem. 61 (37) (2013) 8730–8736.
[28] P.J. Bindu, K.M. Mahadevan, N.D. Satyanarayan, et al., Synthesis and DNA cleavage studies of novel quinoline oxime esters, Bioorg. Med. Chem. Lett. 22 (2) (2012) 898–900.
[29] N.P. Andreou, K. Dafnopoulos, C. Tortopidis, et al., Alkyl and aryl sulfonyl p-pyridine ethanone oximes are efficient DNA photo-cleavage agents, J. Photochem. Photobiol., B 158 (2016) 30–38.
[30] J.R. Hwu, S.C. Tsay, S.C. Hong, et al., Relationship between structure of conjugated oxime esters and their ability to cleave DNA, Bioconjugate Chem. 24 (11) (2013) 1778–1783.
[31] N. Chowdhury, S. Dutta, S. Dasgupta, et al., Synthesis, photophysical, photochemical, DNA cleavage/binding and cytotoxic properties of pyrene oxime ester conjugates, Photochem. Photobiol. Sci. 11 (7) (2012) 1239–1250.
[32] Y. Zhang, Q. Jia, F. Nan, et al., Carbon dots nanophotosensitizers with tunable reactive oxygen species generation for mitochondrion-targeted type I/II photodynamic therapy, Biomaterials 293 (2023) 121953.
[33] X. Liu, Y. Liu, X. Li, et al., ER-targeting PDT converts tumors into in situ therapeutic tumor vaccines, ACS Nano 16 (6) (2022) 9240–9253.
[34] J. Chen, Z. Duan, L. Deng, et al., Cell membrane-targeting type I/II photodynamic therapy combination with FSP1 inhibition for ferroptosis-enhanced photodynamic immunotherapy, Adv. Healthcare Mater. 13 (16) (2024) e2304436.
[35] Z. Yi, X. Qin, L. Zhang, H, et al., Mitochondria-targeting type-I photodrug: harnessing caspase-3 activity for pyroptotic oncotherapy, J. Am. Chem. Soc. 146 (13) (2024) 9413–9421.
[36] Y. Wu, Q. Liu, S. Li, et al., Mitochondria targeting photoredox catalyst-induced pyroptosis for enhanced immunotherapy against hypoxic tumor cells, Chem. Eng. J. 490 (2024) 151599.
[37] J.B. Spinelli, M.C. Haigis, The multifaceted contributions of mitochondria to cellular metabolism, Nat. Cell Biol. 20 (7) (2018) 745–754.
[38] M.J. Devine, J.T. Kittler, Mitochondria at the neuronal presynapse in health and disease, Nat. Rev. Neurosci. 19 (2) (2018) 63–80.
[39] J.E. Chipuk, J.N. Mohammed, J.D. Gelles, et al., Mechanistic connections between mitochondrial biology and regulated cell death, Dev. Cell 56 (9) (2021) 1221–1233.
[40] Y. Yang, P.Y. Liu, W. Bao, et al., Hydrogen inhibits endometrial cancer growth via a ROS/NLRP3/caspase-1/GSDMD-mediated pyroptotic pathway, BMC Cancer 20 (1) (2020) 28.
[41] Y. Wang, P. Shi, Q. Chen, et al., Mitochondrial ROS promote macrophage pyroptosis by inducing GSDMD oxidation, J. Mol. Cell Biol. 11 (12) (2019) 1069–1082.

[42] Kenry, C. Chen, B. Liu, Enhancing the performance of pure organic room-temperature phosphorescent luminophores, Nat. Commun. 10 (1) (2019) 2111.
[43] C. Xiang, Y. Liu, Q. Ding, et al., Precise molecular engineering of multi-suborganelle targeted NIR type-I AIE photosensitizer and design of cell membrane-anchored anti-tumor pyroptosis vaccine, Adv. Funct. Mater. (2024), https://doi.org/10.1002/adfm.202417979.
[44] L. Zhou, L. Fan, F.M. Zhang, et al., Hybrid gelatin/oxidized chondroitin sulfate hydrogels incorporating bioactive glass nanoparticles with enhanced mechanical properties, mineralization, and osteogenic differentiation, Bioact. Mater. 6 (3) (2021) 890–904.
[45] X. Xue, Y. Hu, S. Wang, et al., Fabrication of physical and chemical crosslinked hydrogels for bone tissue engineering, Bioact. Mater. 12 (2022) 327–339.
[46] N. Liu, S. Zhu, Y. Deng, et al., Construction of multifunctional hydrogel with metal-polyphenol capsules for infected full-thickness skin wound healing, Bioact. Mater. 24 (2023) 69–80.
[47] S.H. Kim, H. Hong, O. Ajiteru, et al., 3D bioprinted silk fibroin hydrogels for tissue engineering, Nat. Protoc. 16 (12) (2021) 5484–5532.
[48] J. Feng, Y. Zhang, D. Zhu, et al., Study on the photoinitiation mechanism of carbazole-based oxime esters (OXEs) as novel photoinitiators for free radical photopolymerization under near UV/visible-light irradiation exposure and the application of 3D printing, Eur. Polym. J. 202 (2024) 112662.
[49] Z. Liu, Y. Zhang, J. Feng, et al., Synthesis of carbazole-chalcone bis-oxime esters (CCBOEs) as blue light photoinitiators of polymerization, Polym. Chem. 15 (26) (2024) 2642–2651.
[50] Y. Ding, S. Jiang, Y. Gao, et al., Photochromic polymers based on fluorophenyl oxime ester photoinitiators as photoswitchable molecules, Macromolecules 53 (14) (2020) 5701–5710.
[51] S. Zhu, C. Yu, N. Liu, et al., Injectable conductive gelatin methacrylate/oxidized dextran hydrogel encapsulating umbilical cord mesenchymal stem cells for myocardial infarction treatment, Bioact. Mater. 13 (2022) 119–134.
[52] N. Rajabi, A. Rezaei, M. Kharaziha, et al., Recent advances on bioprinted gelatin methacrylate-based hydrogels for tissue repair, Tissue, Eng. Part. A. 27 (11–12) (2021) 679–702.
[53] C. Liu, Q. Yu, Z. Yuan, et al., Engineering the viscoelasticity of gelatin methacryloyl (GelMA) hydrogels via small "dynamic bridges" to regulate BMSC behaviors for osteochondral regeneration, Bioact. Mater. 25 (2023) 445–459.
[54] S. Zhu, C. Yu, M. Zhao, et al., Histatin-1 loaded multifunctional, adhesive and conductive biomolecular hydrogel to treat diabetic wound, Int. J. Biol. Macromol. 209 (Pt A) (2022) 1020–1031.
[55] R. Miao, C. Jiang, W.Y. Chang, et al., Gasdermin D permeabilization of mitochondrial inner and outer membranes accelerates and enhances pyroptosis, Immunity 56 (11) (2023) 2523–2541.
[56] B.E. Burdette, A.N. Esparza, H. Zhu, et al., Gasdermin D in pyroptosis, Acta Pharm. Sin. B 11 (9) (2021) 2768–2782.